MASTER

Structural characteristics of Co/Ni, Co/Ag, and Co/Cu multilayers measured with nuclear magnetic resonance

te Velthuis, S.G.E.

Award date:
1993

411068

Eindhoven University of Technology (EUT)
Department of Physics
Solid State Division
Group Cooperative Phenomena

Structural Characteristics of Co/Ni, Co/Ag, and Co/Cu Multilayers Measured with Nuclear Magnetic Resonance

S.G.E. te Velthuis

June 1993

Report of a graduation research project carried out in the group Cooperative Phenomena of the Eindhoven University of Technology (EUT).

Supervisor	:	Ir. E.A.M. van Alphen
Professor	:	Prof. dr. ir. W.J.M. de Jonge

The research on magnetic multilayers described in this report is part of a joint project of EUT and Philips Research Laboratories on magnetic properties of metallic magnetic multilayers. Part of the research has been funded by the EEC (SCIENCE and Esprit Basic).

Abstract

Nuclear magnetic resonance (NMR) has been used to make a study of Co/Ni, Co/Ag, and Co/Cu multilayers. A study of structural characteristics such as crystal structure, strain, and interface roughness was made.

The bulk Co structure in Co/Ni multilayers is mainly fcc. In Co/Ag multilayers there is a combination of fcc, hcp and stacking faults.

Principally a study of the strain, which can be determined by measuring the shift in the bulk Co resonance field, was made. It was determined that the studied Co/Ni multilayers (small mismatch between lattice constants) have coherent strain, which means that the layers are uniformly strained throughout the whole layer and that there is lattice registry. The behavior of the strain as a function of both the Co and the Ni layer thicknesses can be described with the coherent model. The results of the Co/Ag multilayers (large mismatch) with various Co and Ag layer thicknesses indicate that there is incoherent strain in the layers, this means that there are dislocations at the interfaces which have relaxed part of the strain. The magnitude of the strain in the Co layer depends primarily on the Co layer thickness. There is qualitative agreement between the results and the incoherent strain model as described by Van der Merwe *et al.*

The resonance lines of Co atoms at the interface (satellites) were determined from the NMR hyperfine field spectra of Co/Ni multilayers. By comparing the intensities of bulk Co to that of Co at the interface, an attempt is made to determine the interface roughness. The interface topology seems to differ amoung some of the samples with various layer thicknesses, so it is not possible to determine the interface roughness, nor can the results be described by any of the proposed interface models.

The ^{63}Cu and ^{65}Cu resonance lines in two Co/Cu multilayers were determined from the NMR spectra and lie at the expected resonance fields.

Contents

Chapter 1

Introduction

Since the development of techniques such as high vacuum evaporation and molecular beam epitaxy, which can be used to grow high quality thin films, there has been a great interest in multilayers. These materials have physical properties such as magnetic anisotropy and giant magnetoresistance that turned out to be very interesting. Besides providing a way to do systematic fundamental research of magnetic properties, magnetic multilayers have several applications. For example, they might be used as magnetic recording devices or sensors. These possible applications are also the basis of the strong cooperation between the EUT and Philips Research Laboratories with respect to magnetic multilayers.

The multilayers investigated are composed of a periodic repetition of two layers of different materials, usually metals. The layers are typically between 5 and 100 Å thick and are repeated up to a hundred times. The layers are usually grown on a substrate with a base layer which can influence the structure of the multilayer. A final layer can be grown on top of the multilayer in order to prevent oxidation. When one of the materials is a magnetic material, the multilayer is referred to as a magnetic multilayer.

The physical properties mentioned above depend strongly on characteristics of the multilayer such as the crystal structure, strain, and interface roughness. Nuclear magnetic resonance (NMR) is a good technique to investigate these characteristics with, because it is sensitive to the local environment of the atoms in the material. Variations of the layer thicknesses change the structure and the strain, thus by examining multilayers with various thicknesses, a systematic investigation is possible. These results can then be related to other physical properties.

This report focusses mainly on the strain in multilayers and the dependence of the strain on the misfit between the materials and the layer thicknesses. Co/Ni and Co/Ag multilayers have been studied for this purpose. The Co/Ni multilayers have a small misfit ($\approx 0.6\%$), which means that it can be expected that the multilayers are coherent for a wide range of layer thicknesses. Co and Ag have a large misfit ($\approx 14\%$), and so Co/Ag multilayers are expected to be incoherent. The strains determined with the experiments are compared with models that exist for both types of strain. The model used in the case of incoherent strain, is the model described by Van der Merwe *et al.* [MER88, JES88].

Besides for a study of the strain, the Co/Ag were grown with the purpose of making a systematic investigation of the interface roughness, anisotropy and magnetoresistance. These studies have been or will be performed by others in the department.

Usually when Co based multilayers are studied, the resonance lines of the Co atoms are investigated, in order to gain information about the hyperfine fields. However, it is also possible to determine the resonance lines of the other element in the multilayer, even if this element does not have a electronic magnetic moment. The Cu resonance lines of two Co/Cu multilayers were determined.

Before the NMR experiments on the multilayers will be described, the effective field felt by the nuclear magnetic moment will be reviewed in chapter 2 and the influence of the environment on this effective field will be discussed in chapter 3. In chapter 4 the principles of NMR along with the experimental apparatus will be described. In chapters 5, 6, and 7 the results of the experiments will be presented along with conclusions and discussions.

Chapter 2

The Effective Magnetic Field

With NMR the interaction between the nuclear magnetic moment of an atom in a material and the effective magnetic field at the nucleus is measured. There are several contributions to this effective magnetic field. In this chapter these contributions will be discussed.

2.1 The Interactions of the Nuclear Moment

A magnetic moment $\vec{\mu}$, when placed in a magnetic field $\vec{B}$, experiences an interaction which can be described by the Zeeman Hamiltonian:

$$\mathcal{H}_z = -\vec{\mu} \cdot \vec{B} \tag{2.1}$$

When the moment is a nuclear magnetic moment with nuclear spin $\vec{I}$, the moment can be written as:

$$\vec{\mu} = \hbar\gamma\vec{I} \tag{2.2}$$

where γ is the nuclear gyromagnetic ratio. The effective magnetic field at the nucleus is the sum of several contributions: a hyperfine field $\vec{B}'_{hf}$, a dipolar field $\vec{B}_{dip}$, possibly an external field $\vec{B}_{appl}$, and an induced field $\vec{B}_{ind}$.

$$\vec{B}_{tot} = \vec{B}'_{hf} + \vec{B}_{dip} + \vec{B}_{appl} + \vec{B}_{ind} \tag{2.3}$$

Thus, the energy difference ΔE between the resulting Zeeman levels is:

$$\Delta E = hf = \hbar\gamma \mid \vec{B}'_{hf} + \vec{B}_{dip} + \vec{B}_{appl} + \vec{B}_{ind} \mid \tag{2.4}$$

where f is the resonance frequency. For ^{59}Co the magnitude of the effective field when the applied field is zero, is in the order of 20 T and $\gamma/2\pi$ = 10.054 MHz/T [WAL67]. The resonance frequency is then in the order of 200 MHz. The various contributions to the total effective field will be discussed in the following sections.

A nucleus with spin $I \neq \frac{1}{2}$ also has a quadrupole moment which interacts with the electric field gradient. This interaction causes an additional separation of the energy levels. However, when the material has a cubic structure there is no effective quadrupole separation. When the material is not cubic the quadrupole separation is often much

smaller than the Zeeman splitting, and only results in a broadening of the spectrum around the hyperfine resonance line. For hcp Co the quadrupole separation is ≈ 0.2 MHz opposed to the 200 MHz Zeeman separation. In summary, fcc Co ($I = \frac{7}{2}$) has no quadrupole separation and hcp Co has a separation that will cause only a small line broadening in the spectrum.

2.2 The Hyperfine Field

The hyperfine field $\vec{B}'_{hf}$ that a nuclear magnetic moment feels, is the sum of three contributions. These contributions are:

1. $\vec{B}_{con}$, the contact field [FER30]
2. $\vec{B}_{dip,at}$, the hyperfine dipolar field due to the spins of the d shell electrons of the atom itself
3. $\vec{B}_{orb}$, the orbital field due to the unquenched part of the orbital angular momentum

The hyperfine field $\vec{B}'_{hf}$ can thus be written as:

$$\vec{B}'_{hf} = \vec{B}_{con} + \vec{B}_{dip,at} + \vec{B}_{orb} \tag{2.5}$$

2.2.1 The Contact Field

The contact field $\vec{B}_{con}$ is the largest part of the hyperfine field. For Co $\vec{B}_{con} \approx 20$ T. It originates from the electrons with a probability density not equal to zero at the nucleus. Electrons which comply with this condition are s type electrons from the inner shells of the atom (core electrons) and from the valence band. One would expect the effective field at the nucleus to be zero because of the pairing of the electrons. However, there is a polarization of the electronic s wave functions. For the core electrons the polarization is caused by the magnetically polarized d shell of the atom. The majority s electrons are pulled toward the d shell, while the minority electrons are pushed away towards the nucleus. The result is a net polarization called the core polarization which is always opposite in sign to the electron magnetization [WAT61, FRE65].

The s valence electrons are also polarized. The conduction electron polarization has two origins. The first is the repopulation of the s valence states because of the presence of the d moment of the atom itself. Secondly, there is a hybridization of the valence s wave functions and the spin polarized d wave functions of neighboring atoms. This also causes a valence s polarization. This polarization is called transferred polarization. The sign and magnitude of the transferred polarization depends strongly on the magnetic moment of the neighboring atoms.

The total contact field $\vec{B}_{con}$ can be described by the expression [ABR62]:

$$B_{con} = \frac{8}{3}\pi\mu_B m(0) \tag{2.6}$$

where $m(0)$ is the spin density within the Thomson radius, at the nucleus [BRE30, BLÜ87] and μ_B the Bohr magneton.

2.2.2 The Hyperfine Dipolar Field

The hyperfine dipolar field is caused by the dipolar interaction of the nuclear magnetic moment and the unpaired $3d$ electrons within the same atom. The local environment of the atom causes spacial deformations of the wave functions of these electrons. When the symmetry of the crystal is cubic, the net hyperfine dipolar field is zero. For lower symmetries, such as hexagonal, the magnitude of the field depends on the angle θ between the c-axis of the material and the electron magnetization. For hexagonal Co the hyperfine dipolar field can be described by [PER65]:

$$B_{dip,at} = B_d \left\{ \frac{3\cos^2\theta - 1}{2} \right\} \tag{2.7}$$

B_d is estimated to be ≈ 0.148 T [PER65].

2.2.3 The Orbital Field

The last contribution to the hyperfine field is the orbital field. The orbital angular momentum of the electrons in the unquenched d shell create this field. The orbital field can be decribed by [PER65, FEK78]:

$$\vec{B}_{orb} = -\frac{\mu_0}{4\pi} g\mu_B \left\langle \frac{\vec{L}}{r^3} \right\rangle \tag{2.8}$$

Here, μ_B is the Bohr magneton, $g \approx 2$ and $\langle \frac{\vec{L}}{r^3} \rangle$ is the expectation value of the angular momentum operator $\vec{L}$ divided by the distance of the electrons to the nucleus r to the third power.

If the crystal symmetry is cubic, the orbitals are quenched and one would not expect an orbital field. However, due to spin-orbit interaction a small orbital moment is induced and thus there is a hyperfine orbital field. This field is parallel to the electron spin moment, thus opposite to the contact hyperfine field. For fcc Co $\vec{B}_{orb} \approx 5$ T [EBE88]. When the crystal symmetry is lower than cubic, the orbital field depends on the direction of $\langle \vec{L} \rangle$ as in equation (2.8). For hcp Co equation (2.8) can be written as [PER65]:

$$B_{orb} = B' + B'' \left\{ \frac{3\cos^2\theta - 1}{2} \right\} \tag{2.9}$$

where θ is the angle between the electron magnetization and the c-axis of the crystal. B' and B'' are estimated to be respectively 11.4 T and 0.418 T [PLO88].

2.3 The Dipolar Field

Besides the hyperfine dipolar interaction between the nuclear magnetic moment and $3d$ electrons of the same atom, the nuclear magnetic moment also has a dipolar interaction

with the (atomic) magnetic moments of all the other atoms. The field created by the other moments can be expressed by:

$$\vec{B}_{dip} = \frac{\mu_0}{4\pi} \sum_i \left[-\frac{\vec{m}_i}{|\vec{r}_i|^3} + \frac{3(\vec{m}_i \cdot \vec{r}_i)\vec{r}_i}{|\vec{r}_i|^5} \right] \tag{2.10}$$

In this equation $\vec{m}_i$ is the magnetic moment of the atom i, $\vec{r}_i$ is the relative position of the dipole i with respect to the nucleus. The summation includes all the dipole moments except that of the atom considered.

The dipolar field $\vec{B}_{dip}$ can be considered as being the sum of a demagnetizing field $\vec{B}_{demag}$ and an isotropic Lorentz field $\vec{B}_L$, which is equal to $\frac{1}{3}\mu_0 M_s$ [COL71]. M_s is the saturation value of the electron magnetization. Measured values of $\mu_0 M_s$ for Co at 4.2 K are 1.79 T [RIE87] and 1.85 T [LAN86]. The demagnetizing field is anisotropic and depends on the shape of the solid and possibly the crystal structure.

In the case of a film, the demagnetizing field can be described using an infinite thin plate approximation. The dipolar field can then be described by:

$$\vec{B}_{dip} = \vec{B}_L + \vec{B}_{demag} = \frac{1}{3}\mu_0 \vec{M}_s - \mu_0 M_s \cos\theta \vec{e}_z \tag{2.11}$$

Here θ is the angle between $\vec{M}_s$ and the normal of the film, whose direction is indicated by the unit vector $\vec{e}_z$.

2.4 The Induced Field

The induced field $\vec{B}_{ind}$ is the result of Pauli spin paramagnetism, orbital paramagnetism and closed shell diamagnetism, which are induced by the applied field $\vec{B}_{appl}$ [WAL67]. For magnetically ordered materials this term is much smaller than the other field contributions. Usually it is neglected, or incorperated in equation (2.4) by omitting the term $\vec{B}_{ind}$ and replacing the gyromagnetic ratio γ by an effective gyromagnetic ration γ_{eff}. In the case of Co, $\gamma/2\pi \approx 10.054$ MHz/T [WAL67] and $\gamma_{eff}/2\pi \approx 10.25$ MHz/T [FEK76]. In paramagnetic materials $\vec{B}_{ind}$ becomes the dominant term in the effective field equation and its effect can be seen in various metals as the Knight shift [SLI90].

Chapter 3

Influences of the Environment on the Hyperfine Field

The magnitude of the contributions to the hyperfine field, as discussed in the previous chapter, are influenced by the characteristics of the local environment such as structure, strain, and the presence of foreign neighbors. In this chapter these influences will be discussed.

3.1 Structure

As indicated in the previous chapter, the magnitude and the orientation of the orbital and dipolar hyperfine fields are influenced by the crystal structure, thus causing the hyperfine field to depend on the structure. The structure determines the magnitude of the hyperfine field and whether it is isotropic or anisotropic. For example, the hyperfine field $B_{hf}(= B'_{hf} - B_L)$ of fcc Co is isotropic and has a magnitude of 21.6 T and hcp Co has an anisotropic hyperfine field B_{hf} of about 22.2 T Because of this difference in hyperfine fields, the structure of a layer can be determined from a measurement of the hyperfine field.

A method of investigating the anistropy of the hyperfine field is by varying the direction of the electron magnetization by varying the direction of the applied field. The direction of the hyperfine field will follow that of the electron magnetization and its magnitude can then be determined as a function of the direction. Unfortunately, this is not as easy as it seems. Because of the anisotropy of the electron magnetization, its direction is not always parallel to that of the applied field. This means that the exact direction of the hyperfine field being detected is not known. Only when the applied field is parallel or perpendicular to the c-axis of the material, will the electron magnetization be parallel to the applied field. By comparing the hyperfine field parallel and perpendicular to the plane of the film or multilayer interface, an approximation of the magnitude of the hyperfine field anisotropy can be made. Another problem that makes anisotropy measurements difficult, is the anisotropy in the dipolar field, which is not always know. Fortunately, in the case of uniaxial symmetry (as in hcp Co) and a thin film, equation (2.11) can be used

to describe the dipolar field. In doing so, equation (2.4) becomes:

$$2\pi f = \gamma(B'_{hf,\parallel} - \frac{1}{3}\mu_0 M_s - B_{appl,\parallel}) \tag{3.1}$$

$$2\pi f = \gamma(B'_{hf,\perp} - \frac{1}{3}\mu_0 M_s + \mu_0 M_s - B_{appl,\perp}) \tag{3.2}$$

Where $\parallel$ and $\perp$ indicate that the field is parallel and perpendicular respectively to the plane of the sample. The resonance field B_{res} is defined as:

$$B_{res} \equiv \frac{2\pi f}{\gamma} + B_{appl} \tag{3.3}$$

A combination of equations (3.1), (3.2) and (3.3) gives:

$$B_{res,\perp} - B_{res,\parallel} = (B'_{hf,\perp} - B'_{hf,\parallel}) + \mu_0 M_s \tag{3.4}$$

In the case of fcc Co, the hyperfine field should be isotropic because the dipolar and orbital hyperfine fields are isotropic. Thus equation (3.4) becomes:

$$B_{res,\perp} - B_{res,\parallel} = \mu_0 M_s \tag{3.5}$$

On the other hand, these terms are anisotropic in hcp Co. The hyperfine field of hcp Co can be written as:

$$B'_{hf} = B_i + B_a \left\{ \frac{3\cos^2\theta - 1}{2} \right\} \tag{3.6}$$

Again θ is the angle between the c-axis and the electron magnetization. B_i is the isotropic and B_a the anisotropic contribution to the hyperfine field. B_a is about -0.57 ± 0.01 T [FEK78]. Equation (3.4) becomes:

$$B_{res,\perp} - B_{res,\parallel} = \frac{3}{2}B_a + \mu_0 M_s \tag{3.7}$$

3.2 Strain

Reflecting on the origins of the hyperfine field, it is clear that it is greatly influenced by the local environment of the nucleus. The dependence of the anisotropy on the crystal structure proves this. In this section the influence of another phenomemon, namely the strain, on the hyperfine field will be discussed. The relationship between the magnitude of the strain and the hyperfine field is characterized by three separate relationships. First of all, there is a relationship between the hyperfine field and an isotropic pressure acting on the material, which will be discussed in section 3.2.1. In a multilayer there are forces at the interface which cause strain as the result of a mismatch between the lattice parameters of the materials. The relationship between these forces and the strain will be described in section 3.2.2. Finally, there are two ways in which a multilayer can be strained. Models for the magnitude of the strain in these two cases will be discussed in the remainder of this section.

3.2.1 The Pressure Dependence of the Hyperfine Field

Strain in a material is the compression or expansion of the lattice caused by forces. It has been shown for Co, Ni, and Fe that there is a relationship between pressure on the lattice causing strain and the magnitude of the hyperfine field [JAN79]. The change in the hyperfine field caused by pressure is the result of two opposing effects. First of all, the net magnetic moment decreases under pressure because of the conversion of d majority spin states into $s-p$ and d minority spin states. This causes a decrease in polarization forces. The decrease in core polarization, thus a decrease in the spin density at the nucleus results in a decrease in the hyperfine field. The opposing effect is caused by the valence s electrons. The $4s$ orbitals are squeezed by the pressure towards the nucleus, thus increasing their spin density at the nucleus. An additional interaction with the core orbitals also increases the density. The result of the increase of the spin density of the valence electrons at the nucleus is an increase of the hyperfine field. The net change in the hyperfine field is the sum of changes of the spin density of the core electrons and of the valence electrons. In the case of Co, the valence contribution is larger, thus the hyperfine field increases when the pressure is increased. The relationship between the hyperfine field and an isotropic pressure P for Co is given by [JAN79]:

$$\frac{\partial}{\partial P} \ln B'_{hf} = 5.92 \cdot 10^{-12} \mathrm{Pa}^{-1} \tag{3.8}$$

The bulk modulus K of a material expresses the relationship between and the change in volume V of a unit lattice cell and the change in pressure P and is given by:

$$\frac{1}{K} = -\frac{1}{V}\left(\frac{\partial V}{\partial P}\right)_T \tag{3.9}$$

For Co, $1/K = 5.26 \cdot 10^{-12}$ Pa^{-1}, at room temperature [LAN86, LAN67, GRO93]. A combination of equations (3.8) and (3.9) gives the relationship between the hyperfine field and the volume V for Co.

$$\frac{\Delta B'_{hf}}{B'_{hf}} = -1.13\frac{\Delta V}{V} \tag{3.10}$$

3.2.2 Strain in a Multilayer

When one material is grown on another material, as in a multilayer, and the lattice constants are not equal, there will be a mismatch at the interface between the two materials. The magnitude of the mismatch is called the misfit η and is given by:

$$\eta = \frac{a_a - a_b}{\frac{1}{2}(a_a + a_b)} \tag{3.11}$$

Where a_a and a_b are the lattice constants of materials a and b respectively, and $a_a > a_b$. In order to accommodate the mismatch at the interface, the layers will become strained. When the layers are strained, the volume of the unit lattice cell will be either smaller or larger than in the unstrained situation, thus leading to a shift in the hyperfine field.

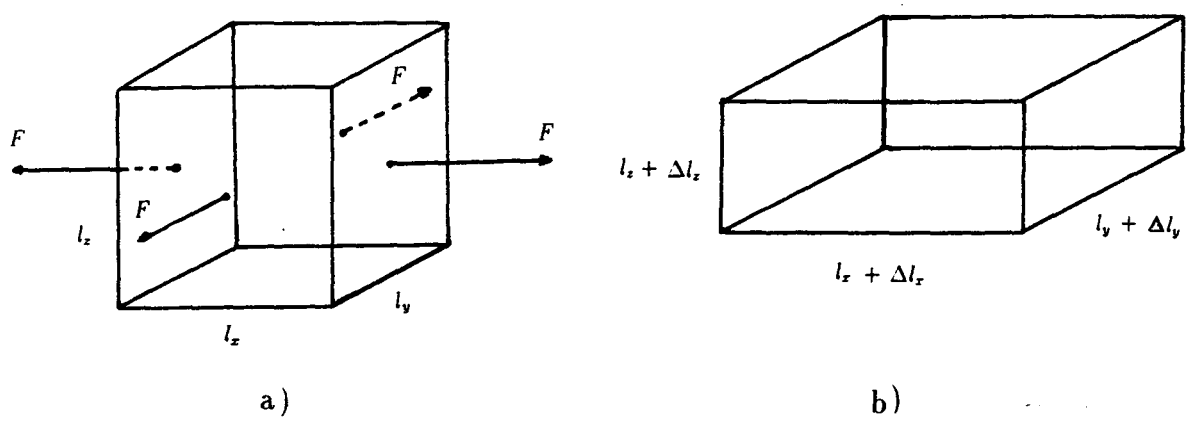

Figure 3.1: *A schematic illustration of a) an unstrained cube with sides l_x, l_y, and l_z, and a) a cube rectangularly distorted by forces F in the x and y directions, σ=1/3.*

The strain is the result of forces in the plane of the interface (in the x and y directions) caused by the interaction between the atoms of the materials. It is assumed that the stresses S (stress is the force per unit area) follow Hooke's law: $S = Ye$, where Y is Young's modulus and e is the strain. In order to understand the change in volume, an elastic isotrope cube with volume V will be considered. According to the theory of elasticity [FEY63], forces in the x direction will, of course, cause a change in the length l_x of the side of the cube, but is will also cause a change in l_y and l_z (see figure 3.1). In the case of interfacial stress there will be forces in both the x and y directions and none in the z direction, resulting in the following normal strains e_i:

$$e_x = \frac{\Delta l_x}{l_x} = -\frac{F}{YA}(1-\sigma) \equiv e \tag{3.12}$$

$$e_y = \frac{\Delta l_y}{l_y} = -\frac{F}{YA}(1-\sigma) = e \tag{3.13}$$

$$e_z = \frac{\Delta l_z}{l_z} = \frac{2F\sigma}{YA} = \frac{-2\sigma}{1-\sigma}e \tag{3.14}$$

Where F is the force, A the area, and σ is the Poisson ratio. Because $\sigma < 0.5$, e_z will be negative when $e > 0$. In this case, the cube's length will increase in the x and y direction, but decrease in the z direction, causing a rectangular distortion. The change in volume is by approximation the sum of the strains in the three directions and can be expressed by:

$$\frac{\Delta V}{V} = e_x + e_y + e_z = \frac{2(1-2\sigma)}{1-\sigma}e \tag{3.15}$$

With equation (3.10) and equation (3.15) the change in the hyperfine field can be related to the strain e.

When there is a mismatch between two materials, there are two ways in which this mismatch can be accommodated. The first way is through coherent strain (section 3.2.3) and the second is through incoherent strain (section 3.2.4). There is a transition from coherent to incoherent when a critical layer thickness t_c (section 3.2.5) is exceeded. When

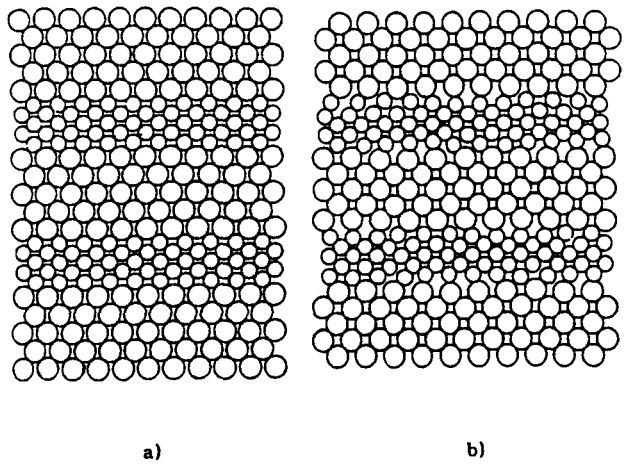

Figure 3.2: *A schematic illustration of a) a coherent strained multilayer and b) an incoherent strained multilayer.*

the misfit is small, it is energetically favorable for the layers to have tensile and compressive strains throughout the whole layer in a way such that the lattice constants in both layers are equal (see figure 3.2). The layers are then called coherent. The strain energy of the layers is in this case proportional to the strained volume. Thus, when the layer thickness increases, the energy also increases. At a certain critical thickness t_c, it will become energetically favorable to introduce misfit dislocations at the interface, which will accommodate part of the misfit, thus relaxing the stress at the interface. The remaining misfit will still be accommodated by strain throughout the layer, but there will no longer be lattice registry at the interface (see figure 3.2). When there is a combination of dislocations and strain, the layers are called incoherent. The energy in this case will be the sum of the energy from the dislocations and the remaining strain. When the misfit is large, t_c will be small, thus even when the layers are relatively thin, they will be incoherent.

In the following sections, models will be discussed which predict the magnitude of the strain e in the case of a coherent and incoherent strained multilayer.

3.2.3 Coherent Strain

The magnitude of the strain in a coherent multilayer depends on the energy needed to strain the layers. When the material is in an equilibrium state, the energy will be minimal. The work w per unit volume of a cubic material that is needed to apply the normal strains e_x, e_y, and e_z is [FEY63]:

$$w = \frac{1}{2}[C_{11}(e_x^2 + e_y^2 + e_z^2) + 2C_{12}(e_x e_y + e_y e_z + e_z e_x)] \tag{3.16}$$

Where C_{11} and C_{12} are the Lamé constants. In an elastic isotropic material they are equal to [FEY63]:

$$C_{11} = \frac{Y}{1+\sigma}\left(1 + \frac{\sigma}{1-2\sigma}\right) \tag{3.17}$$

$$C_{12} = \frac{Y}{1+\sigma}\left(\frac{\sigma}{1-2\sigma}\right) \tag{3.18}$$

Using the expressions for the normal strains from the previous section and the Lamé constants, equation (3.16) becomes:

$$w = 2G\left(\frac{1+\sigma}{1-\sigma}\right)e^2 \tag{3.19}$$

Where G is the shear modulus and $G = Y/2(1+\sigma)$.

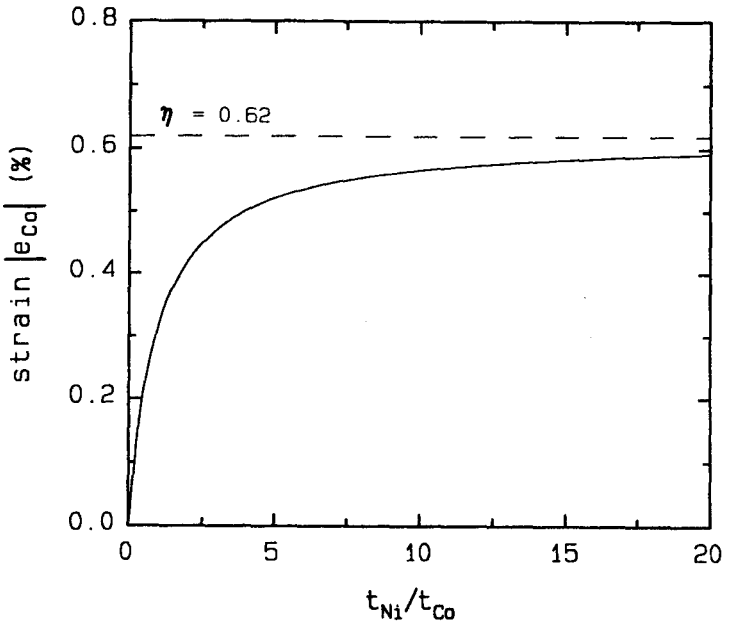

Figure 3.3: *The coherent strain e (in %) in the Co layer as a function of the ratio between the Ni and Co layer thicknesses in a Co/Ni multilayer, calculated with equation (3.21). For a Co/Ni multilayer:* η*=0.62,* a_{Co}*=3.546 Å,* a_{Ni}*=3.524 Å,* G_{Co}*=0.799* 10^{11} *Pa,* G_{Ni}*=0.834* 10^{11} *Pa,* σ_{Co}*=0.310, and* σ_{Ni}*=0.305. The dashed line is the asymptotic limit for the strain which is:* $(a_{Co}+a_{Ni})\eta/2a_{Co} \approx \eta = 0.62\%$.

In a multilayer where the layer thicknesses of materials a and b are t_a and t_b respectively, the total energy E of the coherent multilayer per unit area can then be written as:

$$E_{coh} = 2G_a\left(\frac{1+\sigma_a}{1-\sigma_a}\right)t_a e_a^2 + 2G_b\left(\frac{1+\sigma_b}{1-\sigma_b}\right)t_b e_b^2 \tag{3.20}$$

Minimizing the energy equation with the condition that the lattice constants are equal $(a_a(1+e_a) = a_b(1+e_b))$, the strain in both layers can be determined. The strains in the layers are:

$$e_a = \left(\frac{a_a+a_b}{2a_a}\right)\frac{-\eta}{1+\left(\frac{a_b}{a_a}\right)^2\left(\frac{Z_a}{Z_b}\right)\frac{t_a}{t_b}} \approx \frac{-\eta}{1+\left(\frac{G_a}{G_b}\right)\frac{t_a}{t_b}} \tag{3.21}$$

$$e_b = \left(\frac{a_a+a_b}{2a_b}\right)\frac{\eta}{1+\left(\frac{a_a}{a_b}\right)^2\left(\frac{Z_b}{Z_a}\right)\frac{t_b}{t_a}} \approx \frac{\eta}{1+\left(\frac{G_b}{G_a}\right)\frac{t_b}{t_a}} \tag{3.22}$$

Where $Z_i = G_i(1+\sigma_i)/(1-\sigma_i)$ and $i = a, b$. The approximation is valid when $\sigma_a \approx \sigma_b$ and the misfit is small. Equations (3.21) and (3.22) show that the magnitude of the strain depends primarily on the misfit and the thicknesses of the layers. In figure 3.3 the dependence of the strain e_a as a function of the thickness is shown, where material a is cobalt and material b is nickel.

3.2.4 Incoherent Strain

In this section a way to determine the strain, when the layers are incoherent, will be presented using the model described by Van der Merwe *et al.* [MER88, JES88] for a cubic multilayer.

When the thicknesses of the layers are larger than the critical thickness t_c, which is often the case when the misfit η is large, the layers will be incoherent. This means that there are dislocations at the interfaces which accommodate part of the misfit between the layers. The remaining misfit is accommodated by a strain that is called the misfit strain by Van der Merwe *et al.* The misfit $\bar{\eta}$ accommodated by the dislocations can be written as

$$\bar{\eta} = \eta - \frac{a_a \mid \bar{e}_a \mid + a_b \mid \bar{e}_b \mid}{\frac{1}{2}(a_a + a_b)} \tag{3.23}$$

which for small misfits is equal to the more commonly used expression:

$$\bar{\eta} = \eta - \mid \bar{e}_a \mid - \mid \bar{e}_b \mid \tag{3.24}$$

Where η is the natural misfit and $\bar{e}_a$ and $\bar{e}_b$ are the misfit strains.

The misfit strains are again calculated by minimizing the energy equation of the system with respect to the strains. The energy of the misfit strains E_{ms} can again be calculated with equation (3.20). The difficulty arises when trying to determine the interface energy due to the dislocations. In the literature there are many models for the dislocation energy, although most of them are for thin films grown on a substrate and for relatively small misfits. Most models assume that the lattice and elasticity parameters are the same in both in plane directions (x, y), thus that there is a cross grid of dislocations. The energy of an interface with a one dimensional array of dislocations is E_d. The total energy due to the dislocations at the interface can be approximated by $2E_d$ when the energy of the misfit dislocation crossings in the grid are neglected. It is also assumed that there are no interactions between the dislocations which have a spacing p ($p = a_a a_b/(a_a - a_b)$) between them, and that there is no interaction between the misfit strain and the misfit dislocations so that they can be accounted for independently. The total energy of the system can then be written as:

$$E_{incoh} = E_{ms} + 2E_d \tag{3.25}$$

The model described by Van der Merwe *et al.* [MER88, JES88] uses a succession of parabolic arcs to describe the periodic interaction potential between the atoms across the interface (see figure 3.4). This interaction results in shear and normal stress that are periodic in p (the dislocation spacing) and which depend on the relative displacements of the interfacial atoms with respect to their original positions. In order to account for the

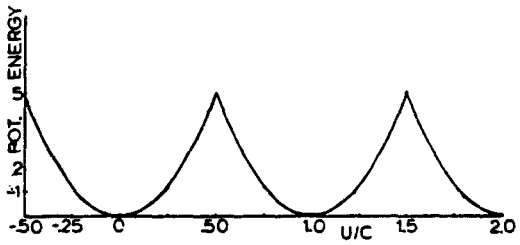

Figure 3.4: *The periodic potential energy as a function of the relative displacement U/c as used by Van der Merwe* et al.*[MER88, JES88] to describe the interaction between the atoms across the interface. The energy unit is $Gc/4\pi^2$, where G is the shear modulus at the interface.*

periodicity of the multilayer, there are boundary conditions for the stresses at the midplane of each layer. The energy associated with the misfit dislocation per unit area interface, can be calculated by determining the work needed for the creation of dislocations. The work is the product of the relative displacements between atoms across the interface U and the forces (stresses) that causes them. The energy E_d can be written as:

$$E_d = \frac{1}{2p}\int_{-p/2}^{p/2} dx \frac{cx}{p} p_{xz}(x) \tag{3.26}$$

Where $p_{xz}(x)$ is the x component of the forces working on the plane perpendicular to the z axis, which is the x, y plane, at the interface. The net relative displacement is cx/p and c is the reference lattice constant ($c = (a_a a_b)/\frac{1}{2}(a_a + a_b)$). The expression for $p_{xz}(x)$ is very complicated and thus the intergral is difficult to calculate. Van der Merwe *et al.* make several simplifications so that a calculation of E_d is possible. Because of the remaining complexity, the simplified expressions for the interfacial stress and the dislocation energy will not be reproduced here (see appendix A).

With a computer program it was possible to calculate the dislocation energy using the simplified expression. Figure 3.5 shows the strain, dislocaton, and total energy as a function of the strain in the Co layer calculated for a Co/Ag multilayer. For more details see [MER88, JES88] and appendix A.

In order to determine the misfit strain the total energy E_{incoh} (equation (3.25)) is minimized with respect to the misfit strain $\bar{e}_a$ and $\bar{e}_b$. This is done by using the additional criterion that the lateral force balance is equal in both layers. This means that:

$$2G_a \frac{(1+\sigma_a)t_a}{(1-\sigma_a)a_a} \mid \bar{e}_a \mid = 2G_b \frac{(1+\sigma_b)t_b}{(1-\sigma_b)a_b} \mid \bar{e}_b \mid \tag{3.27}$$

With this equation the relationship between the misfit strain in the different layers can be written as:

$$\bar{e} \equiv \mid \bar{e}_b \mid = rR \mid \bar{e}_a \mid \tag{3.28}$$

with $r \equiv t_a/t_b$ and

$$R \equiv \frac{(1+\sigma_a)(1-\sigma_b)G_a a_b}{(1-\sigma_a)(1+\sigma_b)G_b a_a} \tag{3.29}$$

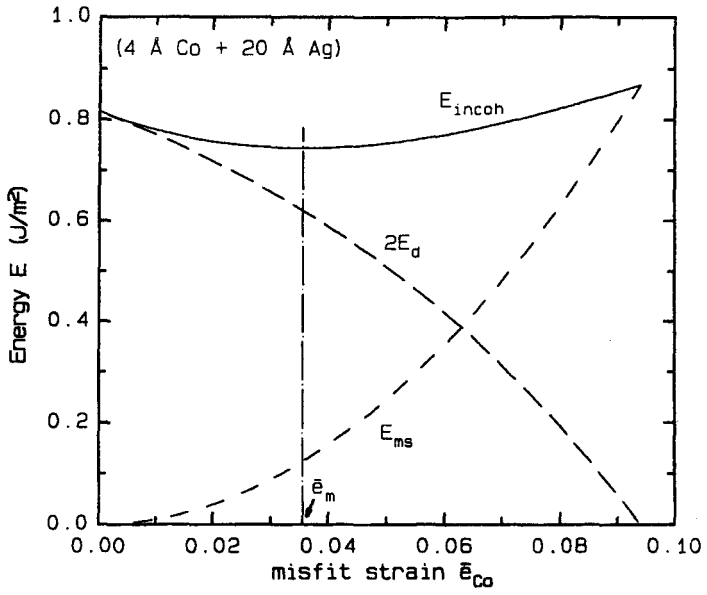

Figure 3.5: *The total energy per unit area of the incoherent multilayer E_{incoh}, which is the sum of the misfit strain energy E_{ms} and twice the dislocation energy $2E_d$, as a function of the misfit strain $\bar{e}_{Co}$, for a multilayer with (4 Å Co + 20 Å Ag). The misfit strain for which the total energy is minimal is $\bar{e}_m$. The elastic constants used in the calculations are listed in table C.1.*

The misfit strain for which the energy is minimal $\bar{e}_m$ can be written as:

$$\bar{e}_m(\bar{\eta}) = CF(\bar{\eta}(\bar{e}_m), E_d(t, \bar{\eta}(\bar{e}_m)), t) \tag{3.30}$$

Where C is a constant and F is a function which depends on the misfit $\bar{\eta}$, the dislocation energy, the thicknesses of the layers ($t = t_b$), and the misfit strain itself. Unfortunately there is no explicite solution for the misfit strains using this model. Thus it is not possible to get a general expression for the misfits strains. However, it is possible to determine the misfit strain for a specific case, when the lattice and elastic constants and the thicknesses of the layers are known. This can be done by numerically calculating the energy E_{incoh} using equations (3.25) and (A.1) for misfit strains $\bar{e}$ ranging from 0 to the maximal value: $\bar{e} = \eta(a_a + a_b)/(2a_b(1 + a_a/a_b rR))$ and then determining $\bar{e}$ for which the energy is minimal ($\bar{e}_m$). By repeating this procedure for various layer thicknesses and making a plot of the results it is possible to see the relationship between the misfit strain and the layer thickness. For a Co/Ag multilayer these calculations have been performed and the results are given in figures 3.6 and 3.7. In these figures the thickness at which the transition from coherent to incoherent strain takes place, is the critical thickness, which will be discussed later on.

At large thicknesses there is a good qualitative agreement with a model previously used in this department for the dislocation energy [MER91]. This model predicts that in the incoherent multilayer, the misfit strain in the Co layer is independent of the other layer thickness and is proportional to $1/t_{Co}$. The accuracy of this model was doubted because

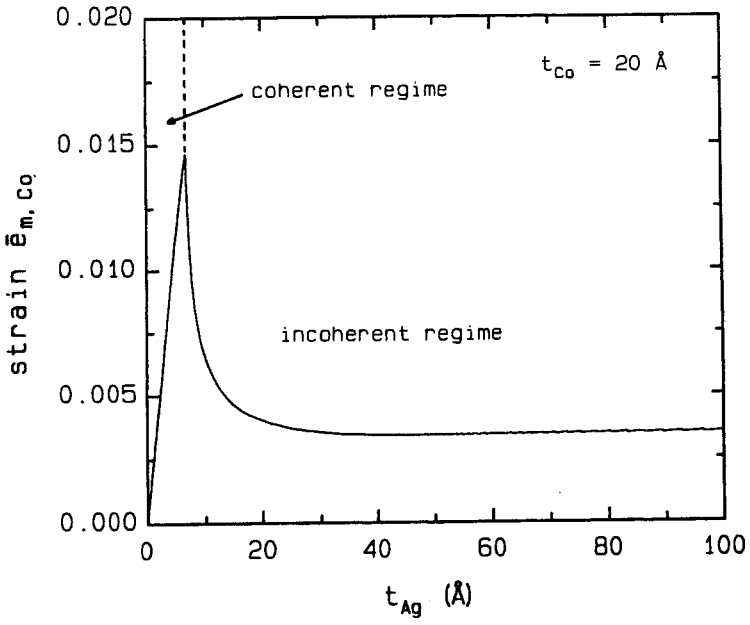

Figure 3.6: *The misfit strain in the Co layer $\bar{e}_{m,Co}$, calculated with the incoherent model, as function of the Ag layer thickness, for a Co/Ag multilayer with 20 Å Co layers. The jagged line for large Ag layer thicknesses is the result of numerical errors made in the determination of the minimal energy. The elastic constants used in the calculations are listed in table C.1.*

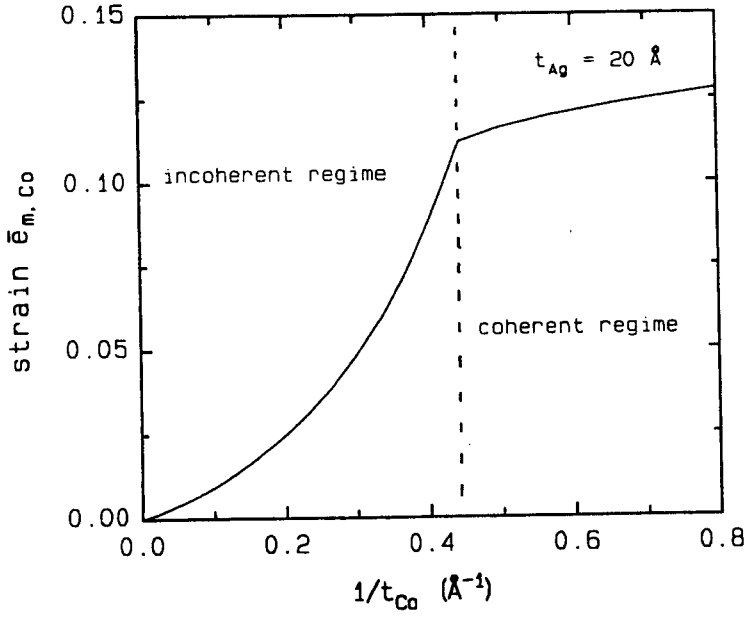

Figure 3.7: *The misfit strain in the Co layer $\bar{e}_{m,Co}$, calculated with the incoherent model, as function of $1/t_{Co}$, for a Co/Ag multilayer with 20 Å Ag layers.*

of the independence of the other layer thickness. This discrepancy was attributed to the fact that equation (3.24) is only a first order approximation for the misfit $\bar{\eta}$.

3.2.5 The Critical Thickness

The transition from a coherent strained multilayer to a incoherent strained layer happens when the thicknesses in the multilayer exceed a certain critical value when the misfit is fixed. Previously these critical values were calculated by assuming that at the critical point, the misfit strain energy was equal to the dislocation energy. Van der Merwe *et al.* use a different assumption to calculate the critical thickness. They state that an incoherent system becomes coherent when the misfit $\bar{\eta} \rightarrow 0$. Which means that there will no longer be any dislocations and only strain will accommodate the misfit and thus: $(a_a \mid \bar{e}_a \mid + a_b \mid \bar{e}_b \mid)/\frac{1}{2}(a_a + a_b) \rightarrow \eta$. This means that at the critical thickness, the misfit strain calculated with the incoherent strain model (equation (3.30)) for $\bar{\eta}$=0 is equal to the coherent strain e (equation (3.22)).

$$\bar{e}_m(0) = CF(0, E_d(t,0), t) = \frac{(1-\sigma_b)}{(1+\sigma_b)}\left(\frac{2a_b}{a_a+a_b}\right)\frac{E_d(t,0)}{2G_b t\bar{\eta}} = \left(\frac{a_a+a_b}{2a_b}\right)\frac{\eta}{1+\frac{a_a}{a_b r R}} = e \tag{3.31}$$

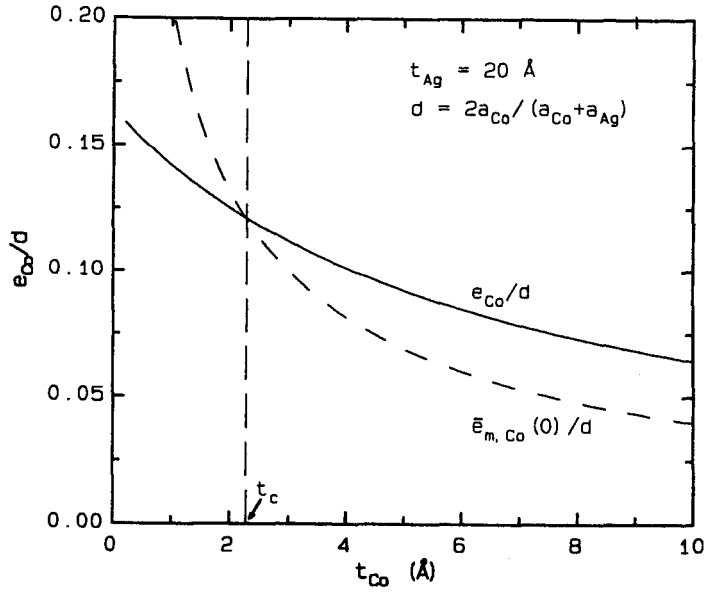

Figure 3.8: *The coherent strain e_{Co} and the misfit strain $\bar{e}_{m,Co}(0)$ (equation (3.31)) in the Co layer both divided by $d = 2a_{Co}/(a_{Co}+a_{Ag})$, calculated for a Co/Ag multilayer with 20 Å Ag layers, as a function of the Co layer thickness. From the intersection of the two curves, the critical Co layer thickness t_c can be determined, t_c=2.3 ± 0.1 Å.*

This relationship is difficult to solve for t_c. An alternative way for determining the critical thickness is by calculating and plotting the misfit strain $\bar{e}_m(0)$ and the strain e, both divided by $2a_b/(a_a + a_b)$ (so that the relationship with $\bar{e}_m$ becomes independent

of the lattice constants), as a function of the thickness t. The thickness at which the two curves intersect is the critical thickness. Figure 3.8 shows the calculated strains for Co/Ag multilayers with 20 Å Ag. From figure 3.8 the critical thickness can be determined. Figure 3.8 shows that the critical thicknesses for this Co/Ag multilayer is 6.7 Å. Similar calculations show that the critical thickness of the Co/Ni and Co/Cu multilayers is much larger than 2000 Å.

3.2.6 Evaluation of the Model

The model provided by Van der Merwe *et al.* provides a method for determining the incoherent strain and the critical thickness specifically for multilayers with a cubic crystal structure and relatively thin layers. In order to do these calculations, several parameters are needed such as the shear moduli, poisson ratios, and lattice constants. The exact influence of these parameters are not know, yet variation in the shear moduli can be expected to have a considerable influence on the results because they are a measure for the bonding of the crystal across the interface. Further numerical investigation is needed to determine the influence of these parameters. Van der Merwe *et al.* define a shear modulus and poisson ratio at the interface of the multilayer. In the calculations done here, the value of these interface parameters are chosen as the average of the parameters of the two materials because of the lack of a better value. It is possible that the real values at the interface are very different. Calculations by Jaszczak *et al.* [JAS90] seem to indicate that this is very likely.

Jaszczak *et al.* also find that the elastic behavior of incoherent strained multilayers show some anomalities. The elastic parameters vary as a function of the periodic multilayer thickness $t_a + t_b$. The numerial values of their calculations cannot be used to correct the parameter values used here because the model for the dislocation is different and they state that their results are purely qualitative. These results indicate that at the most, the qualitative behavior of the dislocation model used here and by Van der Merwe *et al.* can be trusted.

Furthermore, it is neccesary to keep in mind that the model used by Van der Merwe *et al.* is for a small misfit and thin layered multilayer. Also, the periodicity of the multilayers is accounted for only by imposing boundary conditions instead of using periodic functions. The use of parabolic arcs to model the interface potential can also be questioned. Van der Merwe *et al.* suggest that this model best describes systems with shortranged covalent bonded materials (semiconducting materials) and not for multilayers composed of two metals. An other weakness in the model is that is assumes that at the interface the two layers are perfectly smooth, thus that there is not a layer in between that has atoms of both materials. In real multilayers there is always an amount of interface roughness.

All things considered, the model might qualitatively be able to represent the incoherent strain as a function of the thicknesses of the layers, but a quantitative agreement with experiments cannot be expected. Unfortunately this means that the approximation of the critical thickness using this model's equation for the dislocation energy can very well be too large or too small by an order of magnitude.

3.3 Foreign Neighbors and Interfaces

In a multilayer two types of atomic enviroments can be distinguished: bulk and interface environments (see figure 3.9). Bulk atoms are surrounded by atoms of the same kind and are found in the middel of a layer. Interface atoms are only partially surrounded by atoms of the same kind. The other atoms that surround them have different or no magnetic moments, which causes the interface atoms to feel a different hyperfine field than bulk atoms. By studying alloys, the influences of foreign atoms on the hyperfine field can be determined. As stated in the previous chapter, the hyperfine field is the sum of the large contact field and the dipolar and orbital fields. Little is known about the influence of foreign neighbors on the latter two of these fields, so only the influence on the contact field will be discussed here.

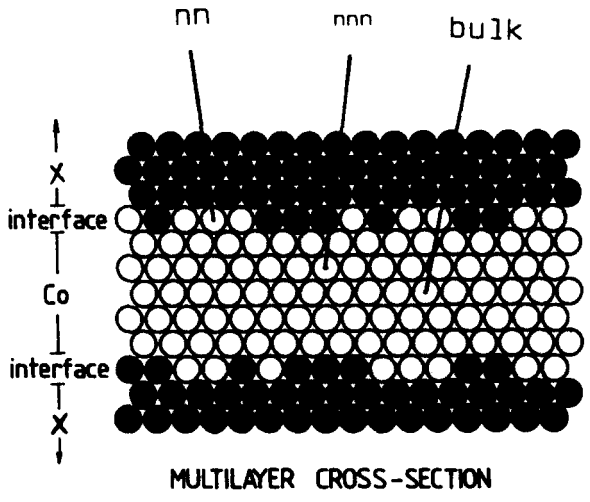

Figure 3.9: *A schematic cross section of a Co/x multilayer. Bulk Co atoms, atoms with one or more foreign nearest neighbors (nn), and atoms with one or more foreign next nearest neighbor (nnn) and only Co nearest neighbors, can be distinguished.*

There are two ways in which a foreign neighbor influences the hyperfine field. First of all, the magnetic moment of the neighboring host atoms changes. Because the 4*s* and 3*d* electrons of the host atoms are not completely localized, these electrons will move slightly in order to regain the charge neutrality, when a foreign neighbor is present and has disrupted the charge neutrality. The magnetic moment of all the atoms is then changed. The change in the magnetic moment of an atom itself changes the core polarization and the repopulation of the valence *s* states, thus changing their contributions to the hyperfine field. Secondly, the transferred polarization, which depends strongly on the magnetic moment of the neighbors, is changed when one neighbor is a foreign neighbor. The influence of this foreign atom on the transferred polarization changes in sign as a function of the distance to the foreign atom. The hyperfine field of the foreign neighbor is also changed when it is present in a different host material and is influenced in the same way.

Although the influence of a foreign atom in a host material can be felt several neighbor

shells away, because of the line widths in a NMR spectrum, only the largest changes in the hyperfine field can be measured. This means that usually only spectral lines of foreign atoms in the nearest neighbor (nn) shells can be distinguished. In the spectra, atoms with one or more foreign atoms in the nn shell can be seen as satellite lines shifted away from the bulk line. This shift can be to the left and to the right of the bulk line, depending of the magnetic moments of the atoms. The distances between satellite lines and the bulk lines should approximately be the same because the addition of each foreign atom to the nn shell should have about the same influence on the hyperfine field.

The intensity of a satellite line is a measure for the number of atoms with a particular surrounding. Because of this, it is possible to estimate the number of interface atoms by comparing the interface intensities to the bulk intensities. A model can be used to predict the relative intensities of the lines with respect to the bulk line when a certain roughness is assumed. By comparing the results of the experiments with models, the interface roughness can thus be estimated. Three models will be explained briefly in the next sections.

3.3.1 The Diffuse Interface Model

The diffuse interface model assumes that at the interface, there are one or more monolayers of atoms where there is a random distribution of the two types of atoms in a certain concentration. An interface monolayer adjacent to bulk material A will have a larger concentration of type A atoms than of type B atoms and vice versa. The intensities are calculated by calculating the probabilities of finding an atom in the interface with a certain environment. These probabilities are determined solely by the concentrations of the atoms in the interface layers.

An atom in layer l has nearest neighbors in layers $i = l+1, l$, and $l-1$. The probability that there are n_i nearest neighbors of type A in layer i for an atom in layer l is:

$$p(z_i, n_i, c_i) = \frac{z_i!}{n_i!(z_i - n_i)!} c_i^{n_i} (1 - c_i)^{z_i - n_i} \tag{3.32}$$

Where z_i is the maximum number of nn sites in layer i and c_i is the concentration of type A atoms in layer i. The total probability of finding an atom of type B in layer l with a certain environment of type A atoms is given by:

$$P(n_{l-1}, n_l, n_{l+1}) = (1 - c_l) \prod_{i=l-1}^{i=l+1} p(z_i, n_i, c_i) \tag{3.33}$$

The intensity of a specific line in the spectrum is determined by the sum over one multilayer period of the probabilities of atoms with the same total number of nn atoms N of type A, where $N = n_{l-1} + n_l + n_{l+1}$.

3.3.2 The Stepped Interface Model

In the second interface model it is assumed that the interface is made up of steps, one or two monolayers deep (see figure 3.10). Two parameters d and l are defined to describe the size of the steps in the plane of the interface. The environment of an atom is determined

by its position with respect to the step. If an atom is at the corner of the step, the number of nn foreign atoms will be different from when it is somewhere in between steps. The number of atoms with certain environments can be determined as a function of d, l, and n, the total number of type B atoms in the whole layer expressed in monolayers.

For one and two step models analytical expressions exist for each satellite (see [GRO92]). With these expressions the intensities of satellite lines I_{sat} and bulk lines I_{bulk} can be compared. For (111) interfaces they are:

One step model:

$$\frac{I_{bulk}}{I_{sat.1} + I_{sat.2}} = \frac{1}{2}d \cdot n - (d + \frac{1}{2}) \tag{3.34}$$

with $n \geq 3, d \geq 2$.

Two step model:

$$\frac{I_{bulk}}{I_{sat.1} + I_{sat.2}} = \frac{1}{3}d \cdot n - \frac{1}{3}(2d + 3) \tag{3.35}$$

with $n \geq 4, d \geq 2$.

The dependence on the parameter l has disappeared in these two examples.

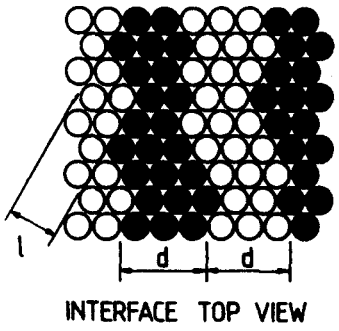

Figure 3.10: *The schematic top view of the interface of a multilayer with mono-atomic steps characterized by the lengths l and d.*

3.3.3 The Hexagonal Island Interface Model

The third interface model is similar to the stepped interface model. Instead of long strips, the interface consists of hexagonal islands of type B atoms (see figure 3.11). The length of the sides of the island is given by l. Furthermore, it is assumed that the number of atoms of type A and B is equal in the mixed interface layer. Again, the number of B type atoms with a certain environment can be determined as a function of l and n, which is again the total number of type B atoms in monolayers. For each satellite there exists an analytical expression. The ratio between the intensities of the bulk line and the first two satellite lines is given by:

$$\frac{I_{bulk}}{I_{sat.1} + I_{sat.2}} = \frac{3l^2 + 3l + 1}{6l + 3}n - (l + 1) \tag{3.36}$$

with $l \geq 2$.

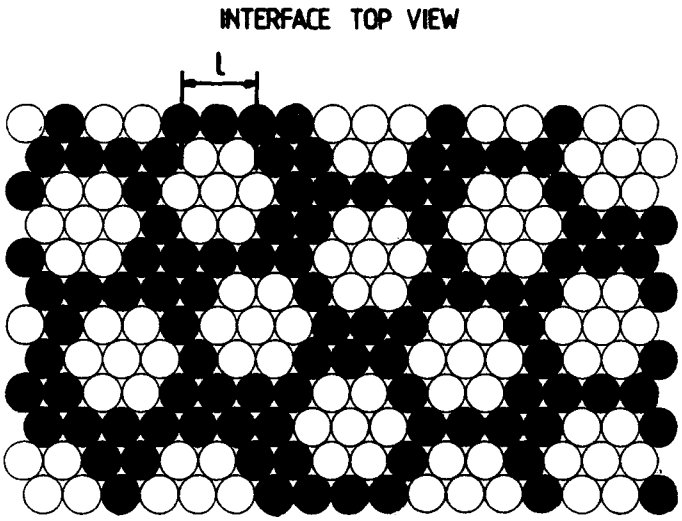

Figure 3.11: *The schematic top view of the interface of a multilayer with hexagonal islands with sides of length l.*

Chapter 4

Experimental Methods and Equipment

In this chapter, spin echo NMR will be discussed. Besides a description of the experimental apparatus, a brief review of the spin echo technique and some related experimental considerations will be given.

4.1 The Principles of Spin Echo NMR

The magnetic moments of the nuclei, in a material, result in a net magnetization $\vec{M}$. When the moments are in a static magnetic field $\vec{B}_0$, the magnetization will be directed parallel to this field $\vec{B}_0$, and will have the saturation value M_0. If the magnetization is disturbed from this equilibrium position it will return with its dynamical behavior described by the Bloch equations [ABR62, SLI90]. If $\vec{B}_0 = B_0\vec{e}_z$ then the Bloch equations are:

$$\frac{d}{dt}M_z = \frac{-(M_z - M_0)}{T_1} \tag{4.1}$$

$$\frac{d}{dt}M_x = \frac{-M_x}{T_2} + \gamma(\vec{M} \times B_0\vec{e}_z)_x \tag{4.2}$$

$$\frac{d}{dt}M_y = \frac{-M_y}{T_2} + \gamma(\vec{M} \times B_0\vec{e}_z)_y \tag{4.3}$$

where γ is the nuclear gyromagnetic ratio. T_1 and T_2 are characteristic relaxation times. The relaxation time T_1 is a result of the interaction of $\vec{M}$ with the lattice and T_2 the result of interactions between spins. During the experiment, a radio frequency (r.f.) magnetic field $\vec{B}_1 = 2B_1\vec{e}_x \cos\omega t$ with frequency ω is added perpendicular to the static field $\vec{B}_0$, which is directed along the z-axis. When the time, during which the r.f. field is applied, is much smaller than T_1 and T_2, no signifcant relaxation takes place and the Bloch equations become:

$$\frac{d}{dt}\vec{M} = \gamma\vec{M} \times (B_0\vec{e}_z + 2B_1\vec{e}_x \cos\omega t) \tag{4.4}$$

For a better understanding it is advantageous to transform the equations of motion to a coordinate frame which is rotating with frequency ω around the z-axis, so that

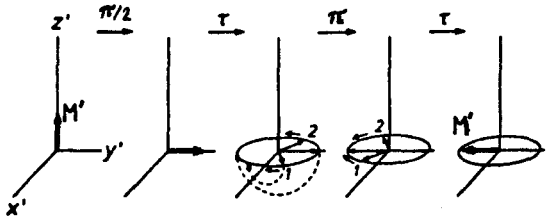

Figure 4.1: *The behavior of the nuclear magnetization $\vec{M}'$ during a $\pi/2-\pi$-pulse sequence. The behavior is given with respect to the rotating frame.*

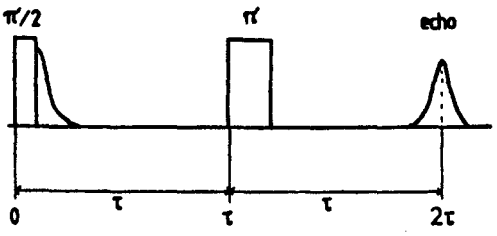

Figure 4.2: *A schematic diagram of a $\pi/2-\pi$-pulse sequence spin echo experiment, where the reaction of the system after the first pulse can also be seen.*

the z'-axis is parallel the the z-axis. In this frame the r.f. field can be written as two components. One component is a static field and the other a high frequency (2ω) field. It can be proven that the influence of the high frequency field can be neglected [HAH50]. The equation of motion (4.4) becomes:

$$\frac{d}{dt}\vec{M}' = \vec{M}' \times [(\gamma B_0 - \omega)\vec{e}_{z'} + \gamma B_1 \vec{e}_{x'}] \tag{4.5}$$

When $\omega \approx \gamma B_0 = \omega_L$ (ω_L is the Larmor frequency), the magnetization will precess mainly around $B_1\vec{e}_{x'}$ in the rotating frame. In the laboratory frame the magnetization spirals up and down the z-axis.

During the experiment the r.f. field is applied for a time τ_p, during which the magnetization will rotate over an angle α with the z'-axis. The angle α is related to the pulse time τ_p as follows: $\alpha = \gamma B_1 \tau_p$.

In a spin echo experiment, two r.f. pulses are applied in sequence. If, for example, the first pulse is a $\pi/2$-pulse (it turns the nuclear magnetization over an angle $\pi/2$), the magnetization will lie in the $x'-y'$ plane after a pulse time τ_p (figure 4.1). Because of field inhomogenities, not all the spins will precess with frequency ω. In the rotating frame this means the spins will precess around the z'-axis in different directions and with different frequencies, and the magnetization will decrease to zero (free induction decay). After a delay time τ a π-pulse is applied, all the spins will rotate in a way such that their angle with the z'-axis is increased by π. This will make the spins refocus after a time τ and the magnetization has a maximum value (figure 4.2). This value is smaller than the value of the magnetization before the experiment because of spin-spin interaction. The induction signal which can be detected because the spins refocus, is called the spin echo.

The actual experiments are done with two pulses of the r.f. field of the same length. In this case, the echo will have a maximum value when $\alpha = 2\pi/3$.

4.2 Experimental Apparatus

A schematic drawing of the experimental apparatus used for the NMR measurements is given in figure 4.3.

The r.f. field is supplied by a MATEC 6600 model generator of which the frequency is adjustable between 1 and 700 MHz. It supplies a power up to $\approx$ 1 kW into 50 Ω. The r.f. signal produced by the MATEC is modulated by a programmable pulse sequence generator. A sequence of two r.f. pulses, each of length τ_p ($\approx 1\mu s$) and separated by τ ($\approx 15\mu s$) is created. The choice of the separation time τ is influenced by T_2 (the spin echo signal decreases with $exp(-t/T_2)$). After passing two 6 dB attenuators and a hybrid TEE the signal reaches the LC-circuit. The attenuators are added to prevent frequency pulling by the r.f. generator, and the hybrid TEE provides 40 dB isolation between the generator output and pre-amplifier input.

The LC-circuit consists of a copper coil that is wrapped tightly around the sample, covering it as much as possible. Both ends of the coil are attached to a capacitor with adjustable capacity (1-65 pF), of which the other end is grounded. The middle of the coil is connected to the 50 Ω coaxial line which is connected to the hybrid TEE.

Besides being used to apply the r.f. field to the sample, the coil is also used to detect the induction signal. The induction signal passes a broad band pre-amplifier before it enters the receiver input. The receiver demodulates the signal and the envelope of the echo appears at the receiver output. The spin echo envelope is displayed directly on a storage oscilloscope (Tektronix 466). The signal is also supplied to a boxcar integrator which performs an analoge averaging, and a data acquisition system (DAS) which enables digital processing of the data with a computer.

The static magnetic field is supplied by a split-pair superconducting magnet, which is placed in a liquid He bath in the cryostat. The sample with the LC-circuit is positioned in the bore of the magnet. It is possible to rotate the sample so that the magnetic field makes an arbitrary angle with the film plane of the sample. The sample is also placed in a liquid He bath, but in a different chamber than the magnet. By pumping the He bath in the sample chamber, a temperature of $\approx$ 1.4 K is achieved during the experiments.

The generator, receiver, and the LC-circuit are all frequency dependent and need to be tuned to the right frequency. This is done with the aid of a very accurate signal generator (HP 8660B signal generator). It replaces the MATEC generator during the tuning of the receiver and LC-circuit because it has a better defined frequency. The LC-circuit is tuned by adjusting the capacity of the variable capacitors. By measuring and minimizing the reflection from the circuit, the circuit is tuned. The HP generator is also used to set the MATEC generator at the desired frequency.

The pulse sequence is usually repeated with a frequency of 10 Hz. In determining the repetition rate, the characteristic relaxation time T_1 has to be taken into consideraton. The boxcar integrator averages the signal for a certain period of time.

The resolution of the apparatus is about 1 MHz and is primarily limited by the band

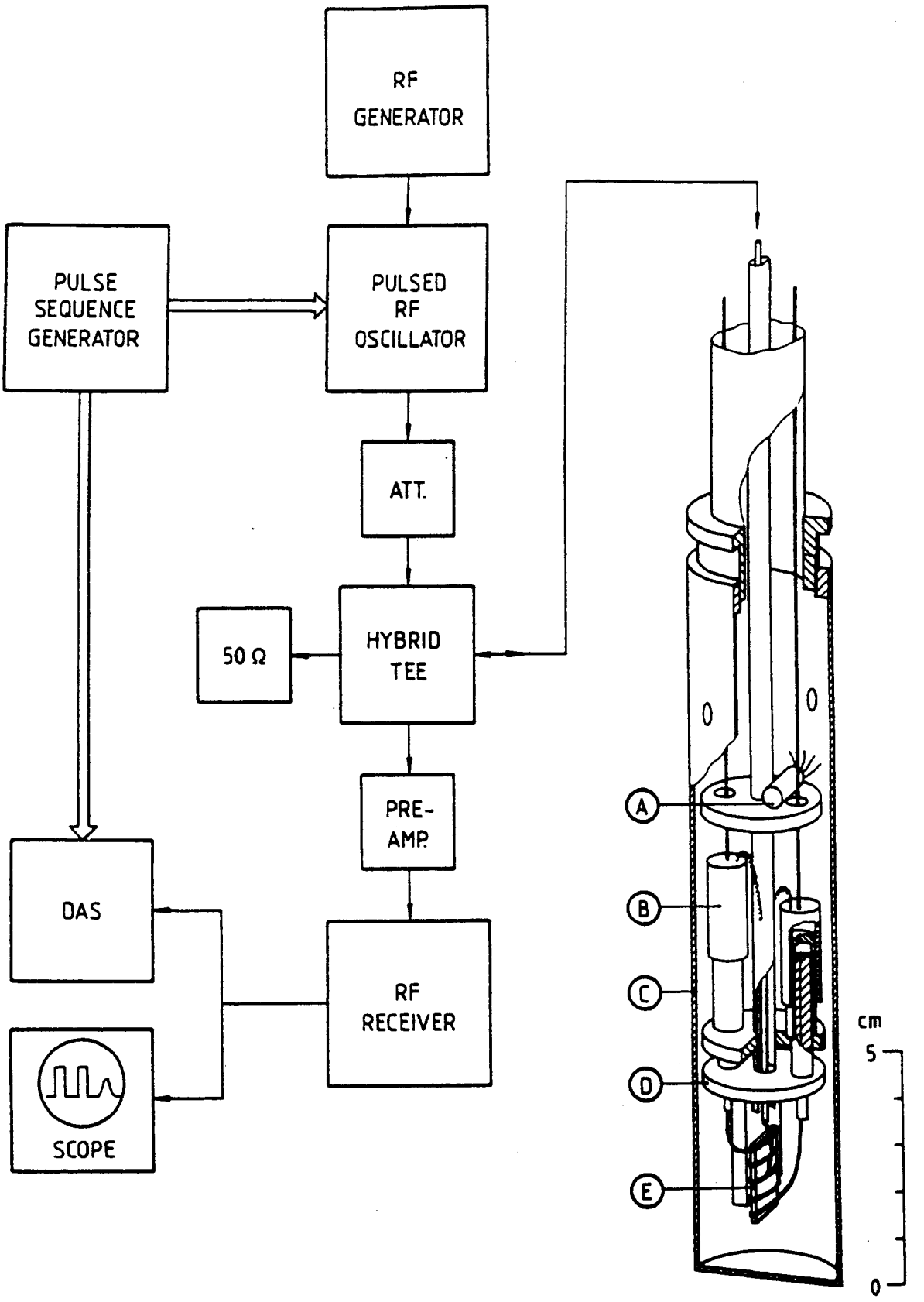

Figure 4.3: *A schematic diagram of the experimental apparatus along with the insert rod on which the sample with the LC circuit is attached: A) carbon-glass resistance thermometer, B) adjustable capacitor, C) shielding D) sample holder E) sample with coil.*

width of the LC-circuit [PLO88].

For a more detailed description of the experimental apparatus see [DEN82, PEL86, KLE87].

4.3 The Spin Echo Measurements

One of the purposes of the spin echo experiment is the determination of the hyperfine fields $\vec{B}'_{hf}$ of a sample. Another point of interest is the determination of the relative amounts of atoms with a certain hyperfine field.

4.3.1 Determination of the Hyperfine Field

When the resonance frequency f and the magnitude of the static applied field $\vec{B}_{appl}$ are known, the hyperfine field can be determined with equation (2.4). If the applied field is parallel to the film plane equation (2.4) becomes:

$$2\pi f = \gamma(B'_{hf} - B_{appl} - B_L) \tag{4.6}$$

The demagnetizing dipolar field $\vec{B}_{demag}$ is equal to zero. For the sake of convenience the sum of $\vec{B}'_{hf}$ and $\vec{B}_L$ was been defined in the previous chapter as the hyperfine field $\vec{B}_{hf}$. With this definition equation (4.6) can be written as:

$$2\pi f = \gamma(B_{hf} - B_{appl}) \tag{4.7}$$

In the case of the applied field parallel to the film plane, the hyperfine field B_{hf} is equal to the resonance field B_{res} also defined in the previous chapter. When the frequency of the r.f. signal is known and constant, it is possible to make a field swept spectrum by varying the applied field. From this spectrum it is possible to determine the hyperfine fields of atoms with different environments in the sample. If the applied field is kept constant (e.g. equal to zero), and the frequency is varied, a frequency spectrum can be made. Again with equation (4.7) B_{hf} can be determined.

Although both methods give the same results, there are practical reasons why it is often preferable to make field spectra instead of frequency spectra. As mentioned in the previous section, the generator, receiver, and the LC-circuit are frequency dependent and need to be retuned at every frequency. This can become a very tedious task when steps of only a few MHz over a range of about 100 MHz are made in order to get a sufficient spectrum. Because of the limited range of the capacitors, the frequency range of the LC-circuit is only about 50 MHz, which means that it is neccesary to replace the coil for one with more or less turns, in order to cover the desired frequency range.

When comparing spectra it is necessary to consider $\vec{B}_{ind}$, which is proportional to the applied field. Although this field is small it can cause significant errors when determining the exact hyperfine field. Thus, when comparing the exact positions of lines in the spectra, it is important that they are measured using the same applied field.

There are cases in which is it preferable to make a frequency spectrum instead of a field spectrum. One of these cases is when the induction signal is small when there is an

applied field. The signal will be much larger in zero field because of enhancement, thus making a zero field frequency spectrum necessary. This enhancement will be discussed further in a following section.

4.3.2 Spin Echo Intensity

The magnitude of the spin echo in an experiment contains information about the number of nuclear spins that are at resonance. Besides this number there are several other parameters that determine the intensity of the echo. Because these parameters may change, it is important to know how the magnitude of the spin echo depends on them.

When the echo is formed, an EMF E is produced in the coil (equation (4.8)) [HOU76]. The spins that produce the echo rotate around $B_0\vec{e}_z$ with a frequency $2\pi f = \gamma B_0$, which is the Larmor frequency.

$$E = K2\pi f B_{1,t} M_t V_s \cos(2\pi f t) \tag{4.8}$$

The phase shift is omitted in equation (4.8). The components of $\vec{B}_1$ and $\vec{M}$, in the sample, perpendicular to $\vec{B}_0$ are respectively $B_{1,t}$ and M_t. K is a factor (≤ 1) that accounts for inhomogenities of B_1 within the sample. V_s is the volume of the sample. M_t is given by [HAH50]:

$$M_t = (1-\eta) M_0 \sin(\alpha) \sin^2(\frac{\alpha}{2}) \exp(\frac{-2\tau}{T_2}) \tag{4.9}$$

with $\alpha = (1-\eta)\gamma B_{1,t}\tau_p$. η is the enhancement factor and will be explained in a following section. The magnetic moment M_0 is the total moment generated by N nuclei per unit volume in a state of thermal equilibrium at a temperature T and can be described by:

$$M_0 = \frac{N\gamma^2\hbar^2 I(I+1)B_0}{3k_B T} \tag{4.10}$$

where I is the nuclear spin angular moment. Equations (4.8), (4.9), and (4.10) show the dependence of the spin echo intensity on several parameters. It follows that the spin echo intensity is proportional to the square of the frequency f, the total number of nuclei at resonance NV_s, and to T^{-1}. There are also dependencies on T_2, η, and K, which will be elaberated on in the following sections.

R.F. Field Inhomogenities

R.f. field inhomogenities effect the spin echo intensity. This effect has been accounted for in equation (4.8) by K. There are two primary sources for these inhomogenities. First of all, the coil around the sample is not perfectly symmetric and has finite measurements. The imperfections in the coil cause a loss of sensitivity in parts of the coil, thus reducing the intensity detected by it. Also, the r.f. field transmitted by the coil will be reduced due to these imperfections. In parts of the sample the r.f. field will not be large enough to cause resonance of the spins. With less spins at resonance there will be less signal to detect. The magnitude of these losses vary as a function of the frequency.

The second source of inhomoginities is the skin effect. The magnitude of the r.f. field will decrease exponentially and only penetrate across a characteristic penetration depth

δ in a sample. This depth is given by [PLO88]:

$$\delta = \left[\frac{2\rho}{\mu\omega}\right]^{\frac{1}{2}} \tag{4.11}$$

where ρ is the specific resistance of the sample, μ the magnetic permeability, and $\omega = 2\pi f$ is the frequency. For Co at 1.4 K with $f = 200$ MHz, the penetration depth δ is about 1000 Å. Besides the fact that in parts of the sample there might not be a r.f. field to excite the nuclear moments, there are again parts where the reduced r.f. field is not large enough to cause full resonance. It must be noted that also the skin depth is a function of the frequency.

Nuclear Spin-Spin Relaxation Time

As equation (4.9) shows, the spin echo intensity depends on the spin-spin relaxation time T_2. Because T_2 represents the interaction between spins of various atoms, atoms surrounded by only atoms of the same kind (bulk atoms) will have a different T_2 than atoms partially surrounded by foreign atoms (interface atoms). When comparing intensities of spectral lines this needs to be taken into consideration.

Enhancement

The electron magnetization causes two types of enhancement. One is called transmitting enhancement and the other receiving enhancement.

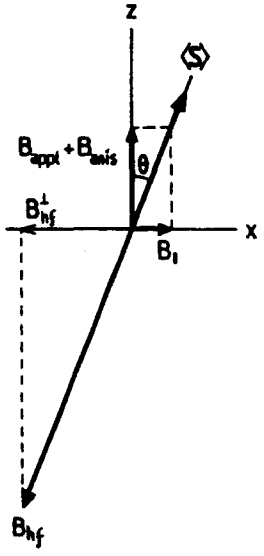

Figure 4.4: *A schematic illustration of the determination of the enhancement factor η.*

Although the electronic resonance frequency is much larger than the nuclear resonance frequency, the r.f. field $\vec{B}_1$ turns the electron spin magnetic moment $\langle \vec{S} \rangle$ over an

angle θ. In the case of a single domain ferromagnet this means that $\vec{B}_{hf}$ will also turn over an angle θ. The total effective r.f. field is [GRO93]:

$$B_{1,eff} = \mid \vec{B}_1 + B_{hf} \sin\theta \vec{e}_x \mid = (1-\eta)B_1 \tag{4.12}$$

with:

$$\eta = \frac{B_{hf}\sin\theta}{B_1} \simeq \frac{B_{hf}}{B_{appl} + B_{anis}} \tag{4.13}$$

if $B_1 \ll B_{appl} + B_{anis}$ (see figure 4.4). B_{anis} is the effective anisotropic field. The r.f. field is thus enhanced by a factor η. The correction for this factor occurs during the experiment by determining the value of τ_p for which the turning angle $\alpha = \frac{2\pi}{3}$. This type of enhancement is called transmitting enhancement.

Receiving enhancement is caused by the hyperfine interaction between the precessing nuclear magnetization and the electronic magnetization. The nuclear spins induce a coherent precession of the electronic magnetization and this enhances the signal produced in the receiver coil by a factor $(1-\eta)$. By dividing the measured signal by $(1-\eta)$, a correction for the receiving enhancement is made.

When there are domains in the material, there is an additional enhancement caused by the displacements of domain walls. In order to avoid having to deal with this type of enhancement, it is preferable to make sure that the material is a single domain. This can be accomplished by applying an external field that is larger than the saturation field.

4.3.3 Determination of the Relative Intensities of Lines

When comparing intensities between lines in a spectrum, it is important to keep in mind the various parameters on which the spin echo intensity depends. As shown in the previous sections, most parameters subsequently depend on the frequency f of the r.f. field. Unfortunately it is not always possible to express this dependence in a mathematical expression. Furthermore, when making a frequency spectrum, the replacement of the coil and the retuning of the apparatus at each frequency causes a change in the sensitivity of the whole set up.

Generally this means that a quantitive comparison of the intensities of different lines in a frequency spectrum is not possible. For this purpose it is better to determine the spectra by varying the field and keeping the frequency constant.

Chapter 5

Co/Ni Multilayers

Co/Ni multilayers are of interest because of the perpendicular magnetic anisotropy which has been observed in them [BLO92, BR092, DAA92]. The anisotropy depends, among other things, on characteristics such as structure, strain, and interface roughness. Two series of Co/Ni multilayers were examined with NMR. One of the series (12 Å Co + x Å Ni) was used to investigate the strain as a function of the nickel thickness. The other series (x Å Co + $2x$ Å Ni) was mainly studied to determine the interface roughness. In this chapter, the results of the NMR study of these samples will be presented. The chapter will end with a discussion of the results.

5.1 Results

5.1.1 25×(12 Å Co + x Å Ni)

A series of ten samples of Co/Ni (111) multilayers was studied. The samples have approximately the same cobalt layer thickness, 12 Å, and various nickel thicknesses (4 Å$\leq x \leq$ 100 Å, see also table 5.1). All samples were grown at Philips Research Laboratories with ultra high vacuum (UHV) vapor deposition with a deposition rate of 0.5 Å/s for both the Co and Ni layers, and with a substraat temperature of 20°C. The multilayers were grown on an oxidized Si substrate with a base layer of 300 Å Au. The substrate and base layer were annealed for 20 minutes at 150°C before the multilayer was grown on top of it.

Field swept spectra were made of all the samples at frequencies of 180 and 190 MHz

25×(12 Å Co + x Å Ni)

Batch number	t_{Ni} (Å)	Batch number	t_{Ni} (Å)
910701	4	910708	21
910702	8	910710	30
910704	10	910711	42
910705	12	910712	60
910706	16	910713	100

Table 5.1: *The layer thicknesses t_{Ni}, in Å, of the examined multilayers.*

with the applied field parallel to the interface plane and at 195 MHz with the applied field perpendicular to the interface plane. The temperature was about 1.4 K for all the experiments. These spectra were made with automatic field sweeps, which means that the resonance condition was fully satisfied only at one point in the spectrum (the optimalization point), usually at the maximum of the bulk line. This means that at a distance from the optimalization point in the spectrum, the intensities of the lines are no longer exactly proportional to the number of atoms with a certain hyperfine field. This can result in a distortion of the shape of the spectral lines at a distance from the optimalization point. For this reason, additional automatic sweeps were made with the resonance condition satisfied near the maximum of the satellite, in order to determine the resonance field of the satellite lines. Only field spectra made by taking small steps in the field and satisfying the resonance condition at every step can be used to make quantitative statements about the relative intensities and the true resonance fields of the spectral lines. This type of spectrum will be called a step wise swept field spectrum. All the spectra were corrected for enhancement.

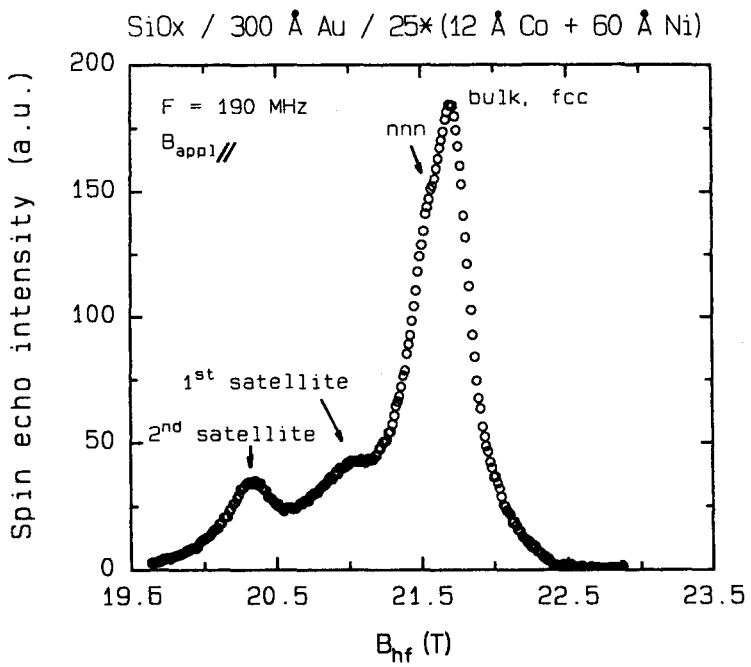

Figure 5.1: *The automatic field swept hyperfine field spectrum of a 25×(12 Å Co + 60 Å Ni) multilayer made at 190 MHz, with the applied field parallel to the interface plane, and at 1.4 K. The spectrum is corrected for receiving enhancement.*

Figure 5.1 shows the automatic field spectrum of a multilayer with 25×(12 Å Co + 60 Å Ni), where the applied field was parallel to the interface plane ($B_{||}$). The spectra of the other samples in the series are very similar. In the spectrum four lines can be distinguished. First of all, the largest contribution can be attributed to the bulk atoms. The resonance field ($B_{res,||} = B_{hf}$) of this line (21.70 T) is close to the hyperfine field value for fcc Co as reported in the literature [RIE68, LAF61] and as measured with NMR experiments of Co films [STE92]. The difference between the hyperfine field of the bulk line in the spectrum and that of bulk fcc Co as reported in the literature, is most likely

the result of strain in the multilayer. On the high field side of the bulk line there is very little intensity, indicating that there are no hcp Co atoms and very little stacking faults. Two satellite lines (20.97 T and 20.27 T) can be distinguished on the low field side of the bulk line. The distance between the bulk line and the first satellite (one nickel atom in the nearest neighbor shell) is approximately the same as the distance between the first and the second satellite (two nickel atoms in the nearest neighbor shell). The second satellite is the most pronounced of the two lines. The difference between the second satellite and bulk line is 1.45 ± 0.05 T, which is the average over all the samples. This separation corresponds to the shift in the hyperfine field measured in Co/Ni alloys, where the concentration of Ni is small [RIE68]. Riedi *et al.* report an average shift of 7.5 MHz = 0.75 T per Ni nearest neighbor. The fourth observable line, which lies approximately 0.2 T lower than the bulk line, was also observed by Riedi *et al.* and La Force *et al.* [LAF61] in diluted alloys and is attributed to Co atoms with no Ni atoms in the nearest neighbor shell and with one or more nickel atoms in the next nearest neighbor (nnn) shell (see also figure 5.4).

The characteristic spin-spin relaxation time T_2 was measured at the resonance fields of the bulk, first satellite, and second satellite contributions of the (12 Å Co + 4 Å Ni) and (12 Å Co + 100 Å Ni) samples. The values of T_2 are 0.3, 0.8, and 0.5 ± 0.1 ms for the bulk, first satellite, and second satellite respectively. It is clear from the difference in T_2 that the lines in the spectrum are the result of Co atoms with different environments. As expected, the relaxation time of the Co with Ni nearest neighbors, thus only partially surrounded by Co spins, is larger than that of the bulk Co, which is completely surrounded by Co spins.

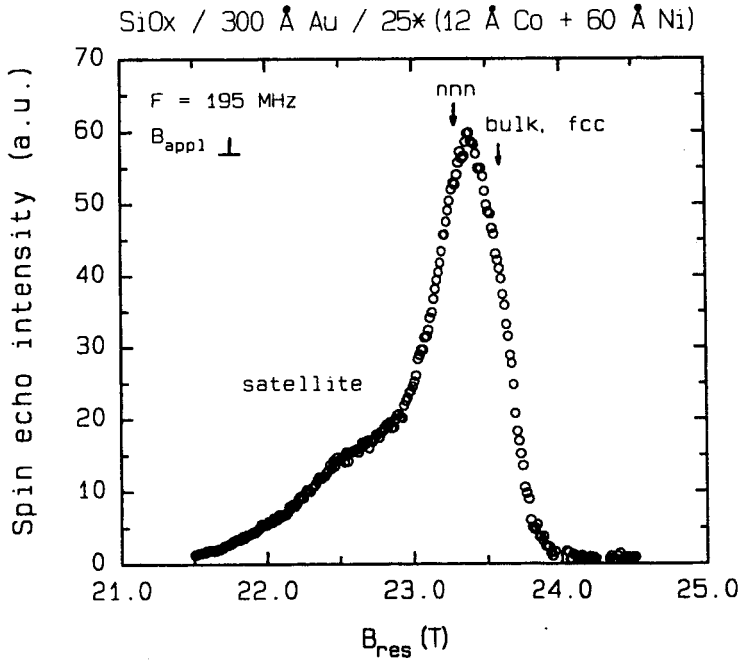

Figure 5.2: *The automatic field swept resonance field spectrum of a 25×(12 Å Co + 60 Å Ni) multilayer made at 195 MHz, with the applied field perpendicular to the interface plane, and at 1.4 K. The spectrum is corrected for receiving enhancement.*

Figure 5.2 shows the spectrum of the same Co/Ni multilayer as in figure 5.1 but now with the applied field perpendicular to the interface plane ($B_\perp$). As expected, the bulk fcc Co line is shifted to a larger resonance field (see equation (3.3)). The difference in the resonance fields of the bulk line when the applied field is perpendicular and parallel to the interface plane, which should be equal to $\mu_0 M_s$ for fcc Co (see equation (3.5)) was determined. Averaged over all the samples, the difference is 1.9 ± 0.1 T. Magnetization measurements of the same samples show that $\mu_0 M_s = 1.80 \pm 0.04$ T [BLO92]. These results also confirm the fact that the Co in the multilayer has the fcc structure.

In figure 5.2 the satellite lines can no longer be clearly distinguished. This is a result of the broadening of the satellite lines. At the interface there is a loss of magnetic symmetry because the magnetic moments of the two materials are not the same. This means that a noticable increase in the quadrupole separation is possible. Furthermore, the dipolar field will be effected by the symmetry loss at the interface. Its influence is the largest when the applied field is perpendicular to the interface plane. These two effects probably cause the line broadening of especially the satellite lines [MER91].

Figure 5.2 also shows that the intensity of the nnn line seems to have become larger than the fcc bulk line. The NMR spectra of Co films which consist of fcc, hcp, and stacking faults indicate that some intensity from the stacking faults comes to lie on the low field side of the fcc line when the applied field is perpendicular to the interface plane [STE92]. Most likely, part of the intensity of the stacking faults, as seen in the spectrum made with the applied field parallel to the interface plane (figure 5.1), is superimposed on the intensity of the nnn line when the field is applied perpendicular to the interface plane, thus making it appear like the intensity of the nnn line has increased.

As mentioned before, the spectra of the different samples were very similar. This is to be expected because the Co layer thickness is approximately the same in all the layers. Thus, the relative intensities of the lines should be the same. Figure 5.3 shows the spectra of three samples (the thickest and thinnest layered samples and one inbetween) from the series, which were made with step wise field sweeps and the applied field parallel to the interface plane. Because the resonance condition was satisfied at every point a quantitative comparison of the intensities is possible. It is obvious that the intensities of the lines measured are not equal in all the samples.

First of all, the 4 Å Ni sample shows more stacking faults and hcp structure on the high field side of the bulk line. Pure bulk cobalt has the hcp structure for temperatures upto 422 °C [ADA68], were a transition to the fcc structure takes place. However, in pure Co films, fcc, hcp, and stacking fault contributions have been observed in various relative intensities depending on the growth conditions and type of substrate [STE92, ALP93]. In the Co/Ni multilayer, the base layer and, more importantly, the Ni layer influences the Co in such a way that the fcc structure is preferred. When the Ni layers become very thin (4 Å $\approx$ 2 monolayers), it can thus be expected that the hcp structure will no longer be totally suppressed.

Figure 5.3 also shows that the intensity of the bulk line with respect to the first two satellite lines is different in these samples. This can only mean that the topology of the interface is different for the samples. Because only part of the interface spectrum is determined, it is not clear whether or not the roughness is different.

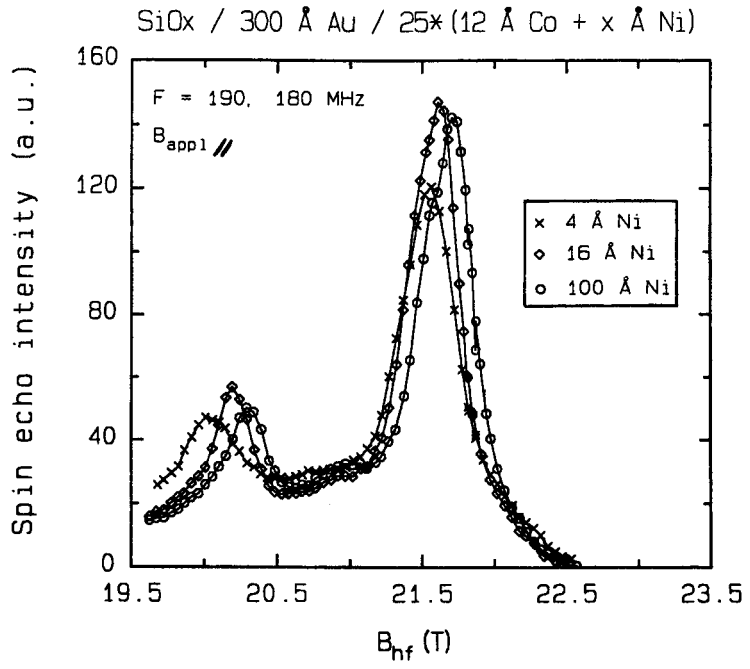

Figure 5.3: *The step wise field swept hyperfine field spectra of three multilayers of the 25×(12 Å Co + x Å Ni) series made with the applied field parallel to the interface plane and at 1.4 K. The spectra are corrected for enhancement. The bulk line was determined at 190 MHz and the interface at 180 MHz. The spectra are normalized so that the total intensities of the spectra are the same.*

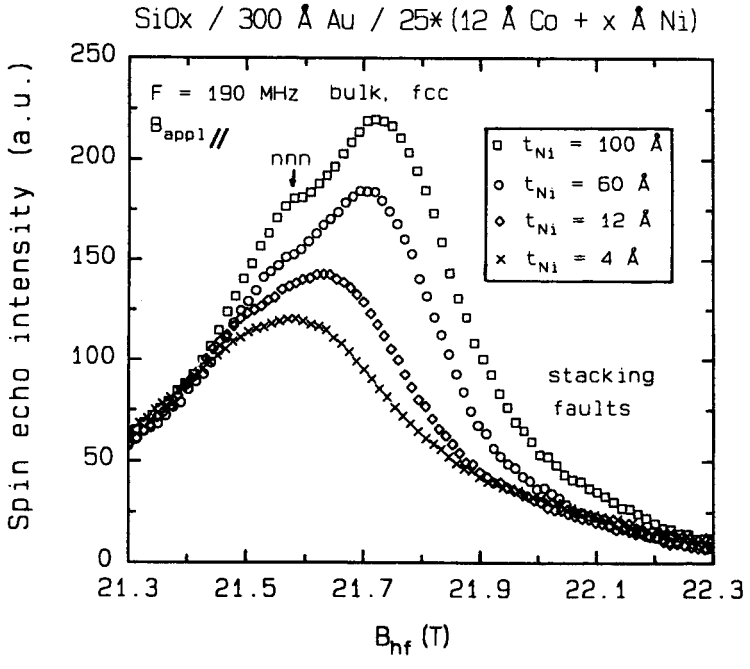

Figure 5.4: *Parts of the automatic field swept hyperfine field spectra of four multilayers of the 25×(12 Å Co + x Å Ni) series made at 190 MHz with the applied field is parallel to the interface plane, and at 1.4 K. The spectra are corrected for receiving enhancement. The spectra are arbitrarily normalized.*

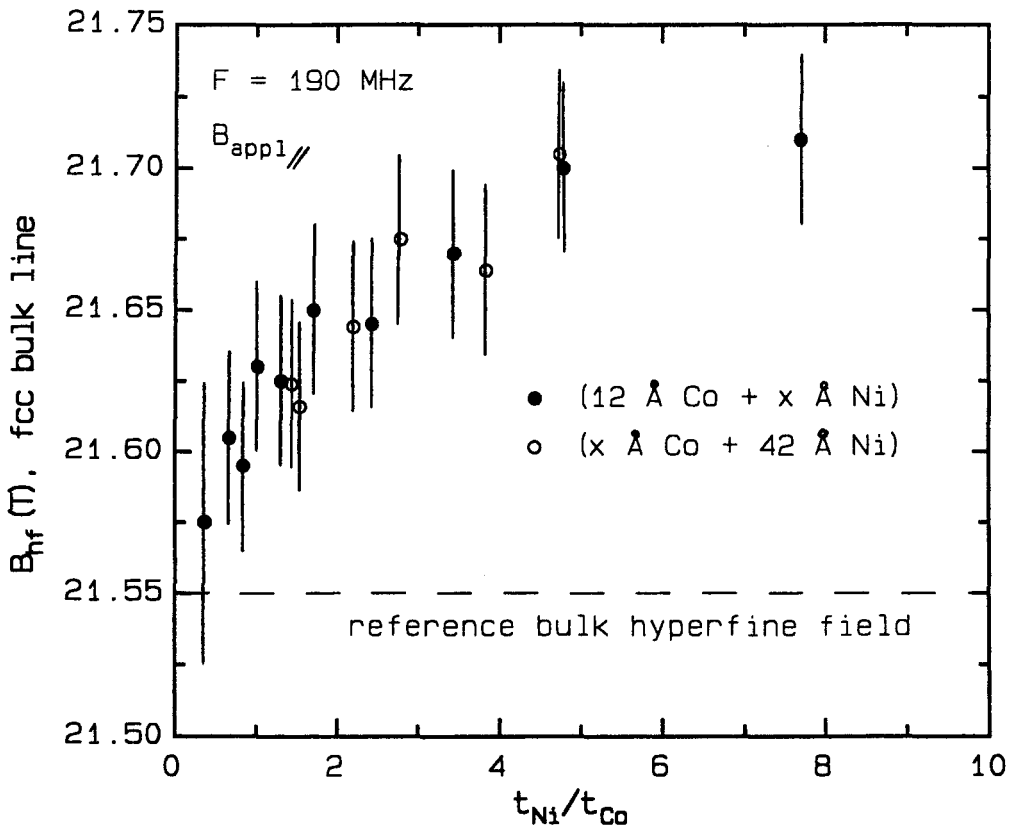

Figure 5.5: *The hyperfine fields of the fcc bulk lines determined from the spectra of the multilayers in the 25×(12 Å Co + x Å Ni) and N×(x Å Co + 42 Å Ni) series which were made at 190 MHz with the applied field parallel to the interface plane, and at 1.4 K, as a function of the Ni and Co layer thicknesses.*

Strain

As figure 5.3 and figure 5.4 show, there is clearly a shift in the resonance field of the spectral lines to a lower field as the nickel thickness is decreased. This is the result of strain, which is the consequence of the misfit (0.62 %) between Co and Ni. The direction of the shift is in accordance with what can be expected when there is compressive strain in the Co layers. Compressive strain in the Co layers is expected because Ni has a smaller lattice constant than Co (a_{Co}=3.546 Å, a_{Ni}=3.5240 Å). Previously in Co/Cu multilayers ($a_{Co} < a_{Cu}$), tensile strain and a shift to higher fields was observed [GRO92b].

The resonance field of the bulk Co line has been determined grafically and by fitting the resonance lines with Gauss curves, from the spectra for each sample and the results are presented in figure 5.5 (see also appendix B). Because of the presence of the nnn line so close to the bulk line and the slight change in the relative intensities of these two lines, the determination of the bulk line resonance field is difficult. The error made in the determination of the resonance field is approximately 0.03 T for almost all the samples.

Figure 5.5 clearly shows a dependence of the resonance field on the Ni thickness. This

indicates that it is more likely that the layers are coherent than incoherent, considering that in the case of incoherent strain, the resonance field would be almost independent of the Ni thickness. This is clearly not the case.

In figure 5.5 the NMR results of a previously studied series of Co/Ni multilayers are also shown. The multilayers of this series all have a Ni layer thickness of 42 Å, yet different Co layer thicknesses. The substrate and base layer of this series is again oxidized Si and 300 Å Au. The growth technique was also the same, only the growth rate of the nickel layers and for some samples also of the cobalt layers was 1 Å/s instead of 0.5 Å/s. The results of this series ($N \times$ (x Å Co + 42 Å Ni); x= 10, 12, 16, 20, 31, 41 Å) agree with the results of the (12 Å Co + x Å Ni) series, as would be expected in the case of coherent strain, because the strain depends on the ratio between the Ni and Co layer thicknesses.

Determination of the critical layer thickness using the method described in section 3.2.5 shows that for both series the critical thickness of the layer that is variable, is much larger than the layer thicknesses of the samples studied. The calculations show that the multilayers should be coherent for layers of at least 2000 Å.

In the case of coherent strain a combination of equations (3.10), (3.15), and (3.21) gives:

$$\frac{\Delta B_{hf}}{B_{hf}} = \frac{C}{1 + Q\frac{t_{Co}}{t_{Ni}}} \tag{5.1}$$

where

$$Q \equiv \frac{a_{Ni}^2 Z_{Co}}{a_{Co}^2 Z_{Ni}} \tag{5.2}$$

$$C \equiv 1.13 \frac{2(1-2\sigma_{Co})}{1-\sigma_{Co}} \frac{a_{Co}+a_{Ni}}{2a_{Co}} \eta \tag{5.3}$$

The parameters C and Q have been calculated using the lattice and elastic constants from tables C.1 and C.2 and are equal to $(8 \pm 1) \cdot 10^{-3}$ and 0.957 ± 0.005 respectively. In this case: $\eta = (6.2 \pm 0.6) \cdot 10^{-3}$.

In order to compare the results with the model for coherent multilayers, the hyperfine field value of the unstrained fcc Co is needed. The hyperfine field of the fcc Co contribution from a 1000 Å Co film with the same substrate (oxidized Si) and grown with a substrate temperature of 20°C, was 21.55 ±0.02 T. The results are compared with this value in order to calculate the relative shift in the hyperfine field $\Delta B_{hf}/B_{hf}$, which is proportional to the strain. In figure 5.6 $\Delta B_{hf}/B_{hf}$ is given as a function of t_{Ni}/t_{Co}. The relative hyperfine field shift for the sample (12 Å Co + 100 Å Ni) is 0.007 ±0.002 which means that the lattice constant of Co has decreased by (0.6 ±0.2)% in the interface plane and increased by (0.5 ±0.2)% in the direction perpendicular to the interface plane. The line in the figure is the result of a fit through the data points. The values of C and Q for the line are $(9 \pm 1) \cdot 10^{-3}$ and 2 ± 1 respectively, and are of the same order of magnitude as the calculated values. The misfit η, calculated from the determined value of C and the elastic and lattice constants from table C.1 and C.2 is equal to $(8 \pm 1) \cdot 10^{-3}$.

The relatively large error in these values has several origins. First of all, there is the error in the determined hyperfine fields (± 0.03 T), although the error in the relative difference in the hyperfine fields of the different samples is smaller. Secondly, the reference hyperfine field is very important. As mentioned, this value is the result of experiments on

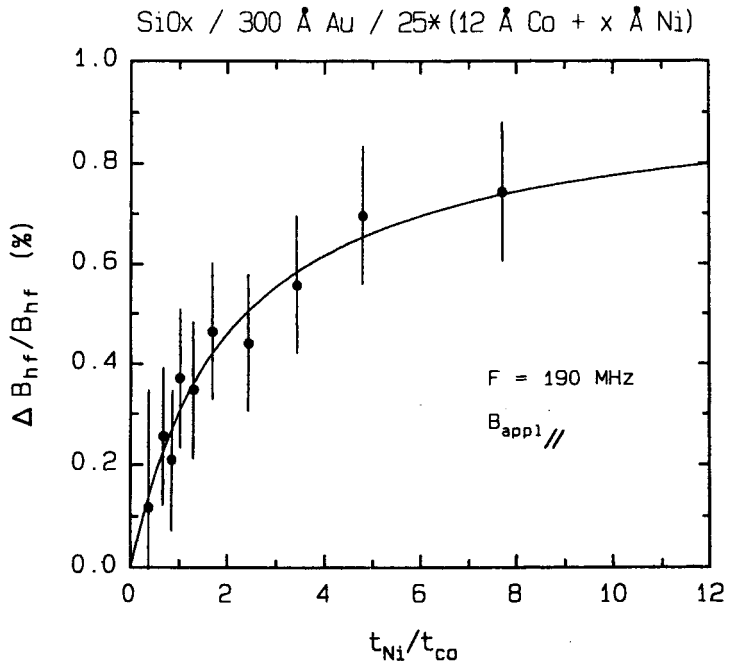

Figure 5.6: *The relative hyperfine field shift $\Delta B_{hf}/B_{hf}$ determined with respect to the reference bulk hyperfine field value of 21.55 T of the 25×(12 Å Co + x Å Ni) series, as a function of t_{Ni}/t_{Co}. The hyperfine fields were determined from spectra made at 190 MHz with the applied field parallel to the interface plane, and at 1.4 K. The line is the best fit of the data points with the coherent strain model with $C = 9.4 \cdot 10^{-3}$ and $Q = 2.1$.*

a 1000 Å Co film. Besides having the fcc structure, the film also has hcp structure and stacking faults. This makes the determination of the exact fcc bulk hyperfine field more difficult. Furthermore, the growth rate of the film and the multilayers was not identical. Thus a certain error in the reference hyperfine field is to be expected. Unfortunately the fit of the data points is sensitive to the bulk reference hyperfine field. A shift of the reference hyperfine field of 0.02 T results in a change of C of $\approx 5\%$ and of Q of $\approx 40\%$.

Besides this problem of determining the correct relative hyperfine field shift, there is an inaccuracy in the predicted values of Q and C. This problem arises from the fact that the lattice and elastic values in table C.1 are all room temperature values while the experiments were done at approximately 1.4 K. It can be expected that the values of these constants will vary with the temperature. Furthermore, these values are bulk matarial values while they are used here to represent relatively thin layered multilayers. It must also be noted that equation (3.10), which gives the relationship between the hyperfine field shift and the change in the volume of a unit cell, holds for an isotropic volume change. The strain in the multilayer is clearly not isotropic (see section 3.2.2).

All things considered, the agreement between the predicted parameter values and the results of the fit of the data points is good enough to conclude that the coherent strain model sufficiently describes the strain in the Co/Ni multilayers.

5.1.2 $N \times (x$ Å Co + $2x$ Å Ni)

A series of Co/Ni (111) multilayers where the Ni layer thickness is twice the Co layer thickness was also studied. The number of repetitions N is such that the total amount of Co is constant, $N \cdot x = 2400$ Å. A list of the samples is given in table 5.2.

N×(x Å Co + $2x$ Å Ni)

Batch number	N	x
915104	40	6
915105	30	8
915106	24	10
915107	20	12
915108	15	16
915109	10	24

Table 5.2: *The layer thicknesses and repetition number of the examined multilayers.*

The substrate on which the layers were grown is mica and the base layer is 200 Å Au which was annealed for 30 minutes at 200 °C. The Co and Ni layers were grown at Philips Research Laboratories with UHV vapor depostion at growth rates of 0.1 Å/s and 0.2 Å/s respectively, while the substrate temperature was 20 °C.

Automatic and step wise field sweeps were made of all the samples with the applied field parallel to the plane of the interface. The step wise sweeps were made in order to study the intensities of the lines so that information about the interface could be obtained. Automatic field sweeps were made of the samples with the applied field perpendicular to the interface plane. Again the temperature at which the experiments were done was approximately 1.4 K.

The difference in resonance field between the bulk line when the applied field was perpendicular and parallel was 1.8 ± 0.1, averaged over the four thickest layered samples.

Interface Roughness

In figure 5.7 the step wise field spectra of the samples are presented. The spectra have been normalized so that the hight of the second satellite line is the same for all the spectra. It is obvious that as the Co layer thickness decreases, the intensity of the bulk line decreases with respect to the interface (second satellite) intensity. It also decreases with respect to the nnn line. This last effect can be observed more clearly in figure 5.8, which gives a portion of the automatic sweept spectra of the same samples. Notable is the fact that in this figure the intensities of the nnn and the bulk lines for the sample with 12 Å Co are almost equal, as is expected when the interface is perfectly smooth.

The relative intensity of the first satellite and the second satellite of the samples with $x = 6$ and $x = 24$ deviates from that of the other samples. The first satellite is larger for $x = 24$ and smaller for $x = 6$. It seems that these two samples have other interface topologies than the other samples. Finally, the spectra seem to have contributions from stacking faults on the high field side of the bulk line. Although in figure 5.7 it seems like the intensity of the stacking faults in the spectrum of the thickest sample is larger than

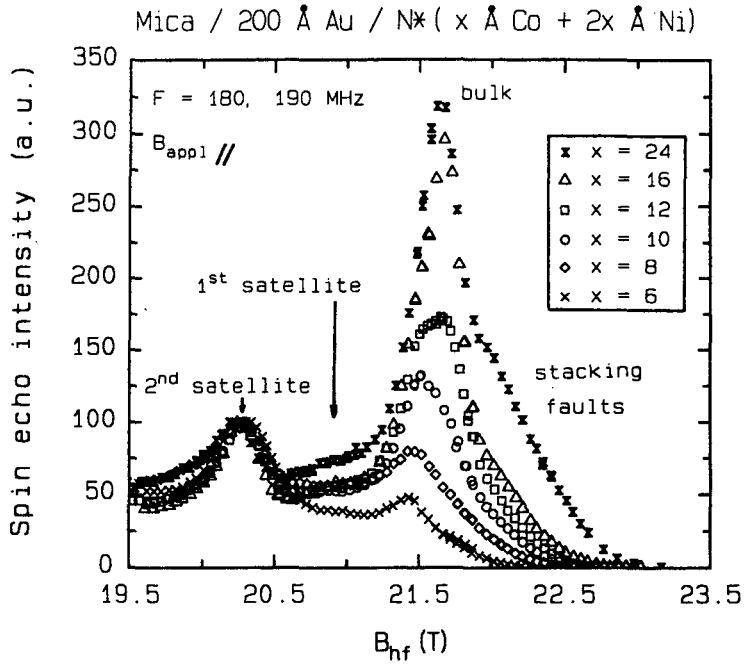

Figure 5.7: *The step wise field swept hyperfine field spectra of the multilayers of the N×(x Å Co + 2x Å Ni) series made with the applied field parallel to the interface plane and at 1.4 K. The spectra are corrected for enhancement. The bulk line was determined at 190 MHz and the interface at 180 MHz. The spectra are normalized so that the hight of second satellite is the same for all the spectra.*

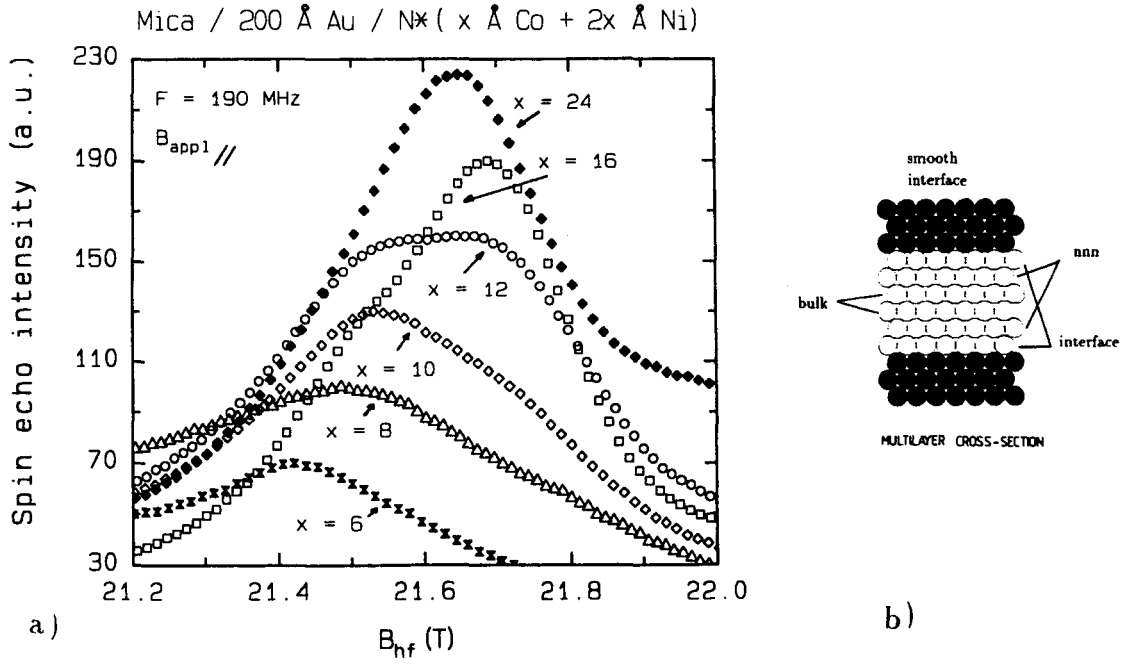

Figure 5.8: *a) Parts of the automatic field swept hyperfine field spectra of the multilayers of the N×(x Å Co + 2x Å Ni) series made at 190 MHz with the applied field is parallel to the interface plane, and at 1.4 K. The spectra are corrected for receiving enhancement. The spectra are arbitrarily normalized. b) A schematic illustration of a multilayer with smooth interfaces. In this case the number of bulk Co and nnn Co atoms is equal.*

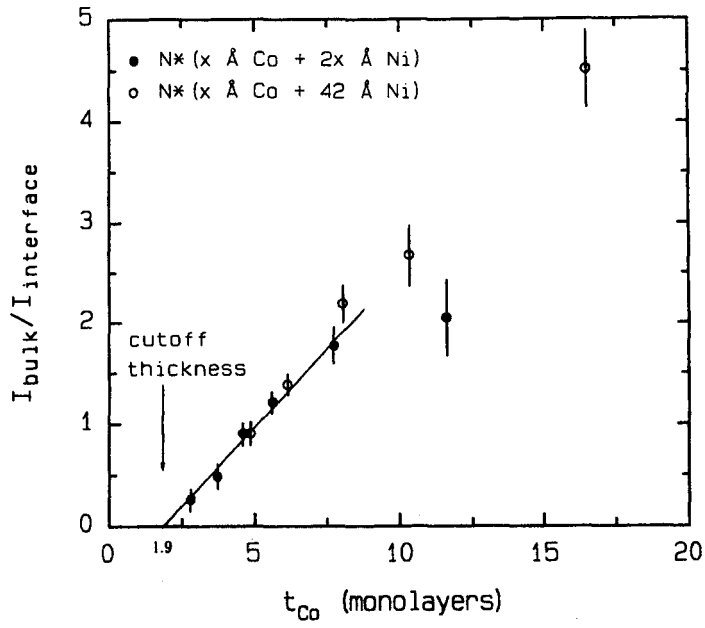

Figure 5.9: *The ratio between the bulk intensity and the interface intensity determined through integration of the spectra of the multilayers of the N×(x Å Co + 2x Å Ni) and N×(x Å Co + 42 Å Ni) series, as a function of the Co layer thickness in monolayers. The spectra were detemined at 180 and 190 MHz with the applied field parallel to the interface plane, and at 1.4 K. The interface intensity is determined by the integration from 19.87 to 21.25 T and the bulk intensity by integration from 21.25 to 23.50 T. The line in the figure is the fit of the data points from the N×(x Å Co + 2x Å Ni) series, excluding the thickest layered sample. The cutoff thickness is 1.9 ± 0.4 monolayers.*

that of the other samples, in fact, its proportion to the fcc bulk is the same in all the samples.

The intensities of the various contributions in the spectra are compared by calculating the intensity under the curve of the spectrum through integration. If the spectral lines had been more pronounced it would have been preferable to fit the curve with the appropriate number of Gauss curves, one for each line. The closeness of the nnn and the bulk line, the stacking faults and the indistinct first satellite makes it impossible to obtain reliable results through this method. Instead it was chosen to divide the spectra into two parts and assigning the lower field part to the interface contribution and the upper field part to the bulk contribution. The separation is made at 21.25 T, just before there is an increase in intensity as the result of the nnn line. Of course there is an error due to the fact that it is impossible to divide the contributions so sharply when the actual spectral lines are so close and clearly overlap each other. Small errors may also arise if there are different strains in the samples which cause the spectra to shift to higher or lower fields.

In figure 5.9 the ratio of the bulk intensity and interface intensity is given as a function of the Co layer thickness in monolayers. As expected there is a linear relationship between the data points. Only the result from the sample with 24 Å Co deviates from the others. This fact agrees with the observation made earlier about the large first satellite intensity for this sample. The ratio of the sample with 6 Å Co for which also a different topology

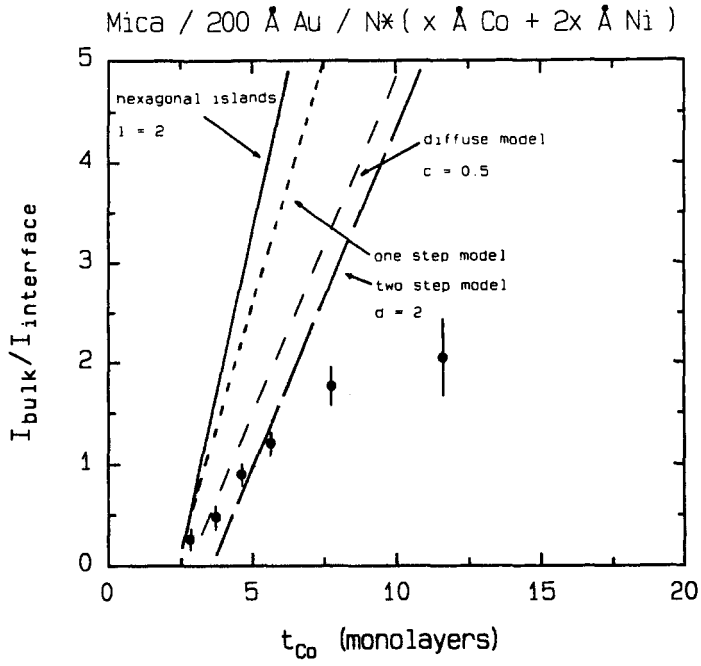

Figure 5.10: *The ratio between the bulk intensity and the interface intensity determined through integration as in figure 5.9 of the multilayers of the $N\times$(x Å Co + 2x Å Ni) series, as a function of the Co layer thickness in monolayers. The lines represent the ratio between the bulk intensity and the sum of the first and second satellite intensities $I_{bulk}/(I_{sat.1} + I_{sat.2})$ as calculated with the one and two step models, diffuse model and the hexagonal island model, which are described in chapter 3.*

was observed, does not seem to deviate from the other results. A line fitted through the data points, with the exception of the 24 Å Co sample, shows that the Co layer thickness at which there is no longer any bulk Co (the cutoff thickness) is about 1.9 ± 0.4 monolayers. This result was also obtained by plotting and fitting the ratio between intensities of the bulk fcc line and the second satellite determined by fitting Gauss curves in the spectra. This result implies that the interfaces are very smooth (the minimal cutoff thickness is 2 monolayers) and that there is approximately one layer of Co at each interface that has Ni atoms in its nearest neighbor shell. The fact that in figure 5.8 the intensities of the nnn and the bulk lines are almost equal, supports this result. However, if the interfaces are as smooth as they seem to be, it would be expected that not the second but the third satellite would be very large and contain most of the interface intensity, and that the first satellite would be absent.

In figure 5.9 also the results of the previously studied series $N \times$ (x Å Co + 42 Å Ni) are shown [GRO92b]. The intensities of the bulk and interface contributions were determined in the same way as for the other series. The data points of this series agree with the results when the layer thicknesses are small.

The results have been compared with the interface models introduced in section 3.3 (see figure 5.10). Neither the stepped interface model, hexagonal island interface model, nor the diffuse interface model is able to describe the results. In all cases the slope of the calculated line is too steep with respect to the actual results. This implies that there are more interface atoms and thus that the interfaces are rougher than is assumed in the

models. In the case of the stepped model the slope is the lowest when the parameter d is equal to 2. For the hexagonal island model this is the case when the parameter l is equal to 2. De slope of the line calculated with the diffuse model is the lowest when the mixed interface layer consists of 50% Co. Although quantitatively the hexagonal island model does not describe the results, for small values of l, the model predicts a large second satellite contribution with respect to the first and third satellites. This is also what the spectra show.

The comparison between the results and the models imply that the samples have rougher interfaces than the cutoff layer thickness indicates. A possible explanation would be that the large second satellite, which would not be expected to be so prominent in the case of very smooth interfaces, is in fact the third satellite. However, the calculations from the models based on this assumption still cannot describe the NMR results.

If the interface roughness of the samples was different amoung the samples, the slope of the line through the data points would change, or more likely, the linear relationship would disappear. A less steep slope such as the data points have, could mean that the interface of the thicker layered samples is rougher.

Because only part of the interface spectrum has been determined, shifts of intensity to other satellites cannot be detected. These shifts could be the result of changes in the topology of the interface, meaning that for example, in the stepped model the parameters d and l were different. These types of shifts could make it appear like the thicker layered samples have rougher interfaces while it would in fact not be the case.

It is clear that the cutoff thickness cannot be used to determine the interface roughness if this roughness or the topology of the interface is different amoung the samples compared, and this seems to be the case in the (x Å Co + $2x$ Å Ni) series.

Strain

According to the coherent strain model the samples in this series should all have the same resonance fields for the various lines because the ratio between the Ni and Co thickness is approximately 2 in all cases. The hyperfine field values of the fcc bulk Co line of the four thickest layered samples seems to contradict this (see table B.2). However, due to the changes in the nnn intensity with respect to the bulk intensity, it is very difficult to determine the hyperfine field very accurately. Furthermore, the position of the second satellite of these samples hardly varies at all, thus supporting the coherent model. The results are not accurate enough to make any definite statements about a possible variation in the strain amoung these multilayers. The only observation which can be made is that the average resonance field of these samples is 21.70 $\pm$0.03 T and lies above the resonance field curve established by the data points from the (12 Å Co + x Å Ni) series. A possible explanation for this discrepancy is the different substrates on which the layers were grown. It has been determined that the resonance field of 1000 Å Co films can be influenced by the substrate temperature during growth and the type of substrate [STE92, ALP93].

5.2 Conclusions

In the NMR spectra of Co/Ni multilayers, four lines can be distinguished in the hyperfine field range examined. Besides a bulk contribution that consists primarily of fcc structured Co, there are two satellite lines from Co with Ni nearest neighbors and one line from Co with one or more Ni next nearest neighbors and only Co nearest neighbors. The average distance between the bulk fcc line and the second satellite is 1.45 ± 0.05 T for the (12 Å Co + x Å Ni) series, which is in agreement with a hyperfine field shift of 0.75 T per Ni nearest neighbor as reported by Riedi *et al.* [RIE68].

The dependence of shifts in the hyperfine fields of the samples of the (12 Å Co + x Å Ni) series, on the Ni layer thickness, is as is described by the coherent strain model, which predicts a dependence of the shift on t_{Ni}/t_{Co}. The results from the previously studied (x Å Co + 42 Å Ni) series are in agreement with these new results. Taking into account the numerous sources for errors in the experimentally determined and the calculated values for C, which is a measure for the misfit, and Q, which is mainly the ratio of the elastic constants of the two materials, there is sufficient qualitative agreement to conclude that the strain in the multilayers of these two series can be fully described by the coherent strain model.

Comparison of the intensities of the resonance lines of three samples of the (12 Å Co + x Å Ni) series indicate that the interface topology of the samples studied is not the same for all the samples. Investigation of the other samples in order to determined a possible Ni layer thickness dependency is not advisable because the differences between the thickest and thinest layered multilayers are small.

The relative intensities of the bulk and interface contributions of multilayers of the (x Å Co + $2x$ Å Ni) series, agree with the previously examined (x Å Co + 42 Å Ni) series, for small layer thicknesses. By calculating a line through the data points, a cutoff thickness is determined, which should indicate the interface roughness. The value of the cutoff thickness (1.9 ± 0.4 monolayers) implies that the interfaces are very sharp. This view is strengthend by the fact that for the sample with 12 Å Co, the nnn and the bulk contributions have almost equal intensities, as would be the case if the interfaces were very smooth. Primarily because not the third but the second satellite is very dominant in all the spectra and also because of the indications that the interface topology of the samples is different, thus making the determined cutoff thickness a meaningless quantity, it is not very likely that the interfaces are sharp.

The relative intensities of the spectral lines of the (x Å Co + $2x$ Å Ni) series can not be described with the diffuse, hexagonal island, or stepped interface models. Furthermore, the models can not explain the dominance of the second satellite as is seen in all the spectra. Possible other interface structures such as Co or Ni non-hexagonal islands in the mixed interface layer could give a better agreement.

In order to determine the interface roughness of one specific sample the whole interface spectrum is neccesary. If only parts of the spectrum is know, it is important that all the samples have the same interface roughness and topology to begin with, or else it is impossible to make an accurate calculation.

The apparent shift in the hyperfine field of the fcc bulk line in the (x Å Co + $2x$ Å Ni) series could be the result of the inaccuracy in determining the resonance field as the

result of the nnn line so close the the fcc line and the change in relative intensity between these two lines in the different samples.

Because both the Co and the Ni layer thicknesses vary in this series, it is difficult to determine whether changes in the various characteristics are the result of the Co or Ni layer thickness. It is preverable to have only one variable in a series.

Chapter 6

Co/Ag Samples

Several Co/Ag multilayers and a Co/Ag diluted alloy were studied with NMR. Because of the perpendicular giant magnetoresistance which has been observed in them [PRA91], Co/Ag multilayers are of great interest. Through the study of an alloy, information about contributions from Co atoms with Ag atoms in the nearest neighbor shell is obtained. These results can be used to understand the Co/Ag multilayer spectra. Most of the Co/Ag multilayers examined are part of a large series which was studied for the purpose of investigating the strain in Co/Ag multilayers as a function of the Co and the Ag layer thicknesses. Due to the large misfit (14%) between the two materials it is expected that there will be incoherent strain. This chapter will start with the results of the NMR measurements of a Co/Ag alloy (2% Ag). In section 6.1.2 the results of an initially grown multilayer (15 Å Co + 9 Å Ag) will be presented. Finally the results of two large series of Co/Ag multilayers ((x Å Co + 20 Å Ag) and (20 Å Co + y Å Ag)) will be described. The chapter will be ended with the conclusions.

6.1 Results

6.1.1 Co + 2% Ag, Alloy

One diluted Co/Ag alloy (sample no. 920801) was examined. The sample was made at Philips Research Laboratories with HV magnetron sputtering at a rate of 2 Å/s at room temperature. 3000 Å Co with 2 mol % Ag was sputtered on a mica substrate. In order to increase the intensity, four identical samples were stacked to make one sample.

Automatic field sweeps of the alloy were made with the applied field parallel and perpendicular to the interface plane. The field swept spectra were corrected for receiving enhancement. Four resonance lines (21.54, 21.81, 22.18, and 22.51 T) can be distinguished belonging to fcc, hcp, and stacking fault structured bulk Co (see figure 6.1). The positions of the lines are in agreement with results from pure Co films which also contain a mixture of these structures [STE92].

In addition to the automatic field sweep, part of the spectrum was determined by making a step wise frequency sweep with zero applied field. Because of the large domain wall enhancement when the applied field is zero, this method was chosen for the part of the spectrum with low hyperfine fields. This enhanced signal is usefull because the

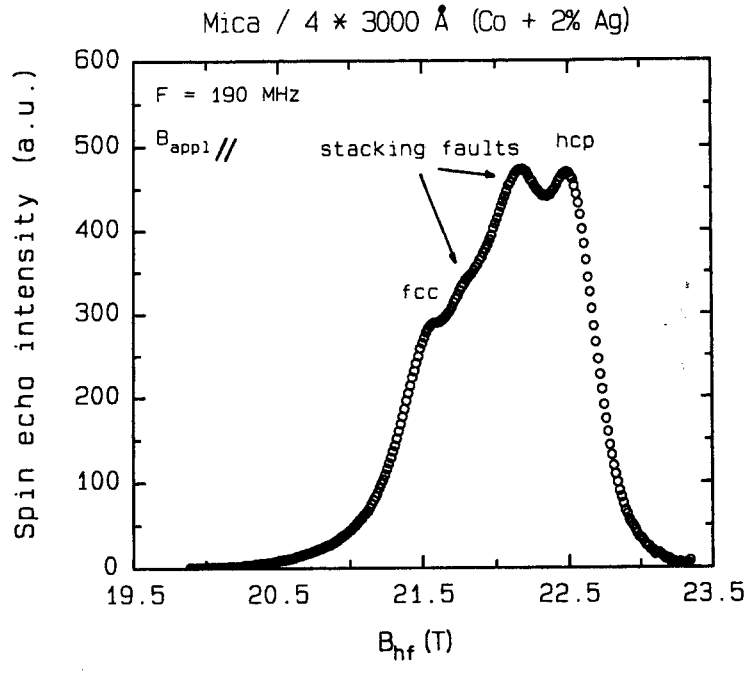

Figure 6.1: *The automatic field swept hyperfine field spectrum of the 4×3000 Å(Co + 2% Ag) alloy made at 190 MHz with the applied field parallel to the interface plane, and at 1.4 K. The spectrum is corrected for receiving enhancement.*

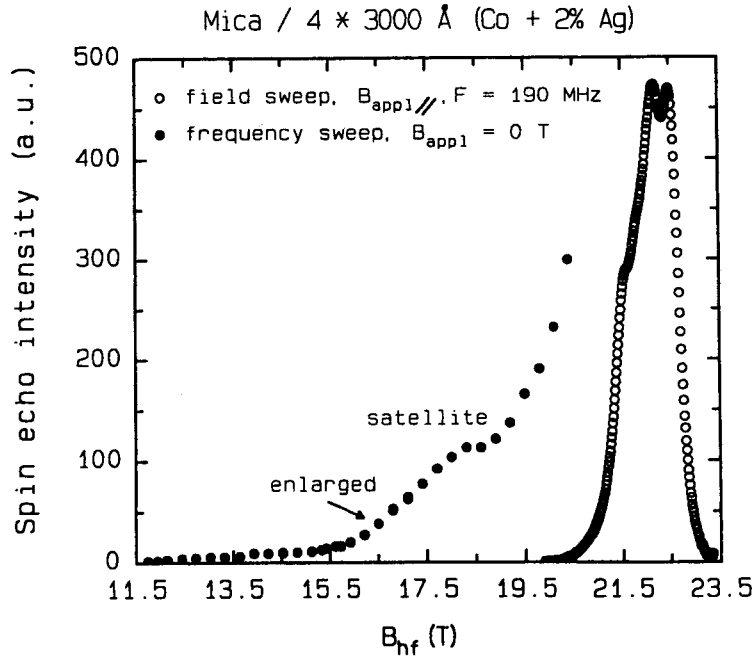

Figure 6.2: *The hyperfine field spectrum of the 4×3000 Å(Co + 2% Ag) alloy made at 1.4 K and partially with a automatic field sweep at 190 MHz with the applied field parallel to the interface plane and partially by a zero applied field frequency sweep. The field swept spectrum is corrected for receiving enhancement and the frequency swept spectrum is corrected for the f^2 dependence of the spin echo intensity.*

intensity of the satellite lines is very small and undetectable when there is an applied field. The frequency swept spectrum was corrected for the f^2 dependence of the spin echo intensity. Figure 6.2 shows the frequency swept spectrum, where the frequency has been transfered into the hyperfine field, along with the automatic field swept spectrum for which the applied field was parallel.

At least one satellite can be distinguished at a hyperfine field of 18.4 ± 0.1 T. The distance between the fcc bulk Co line and the satellite is 3.1 ± 0.1 T.

If the 2% Ag had been evenly spread throughout the Co, the ratio between the bulk and first satellite intensity would be about 3 and only the first satellite would be present. Because the intensity of the bulk Co is much larger than that of the satellite, the Ag in the alloy is probably clustered in the alloy. This is very likely because Co and Ag are immiscible. If the satellite that can be seen is not the first satellite, the Ag atoms will definitely be clustered, because only if there is clustering is it possible that the Co will have two or more Ag nearest neighbors.

6.1.2 60×(15 Å Co + 9 Å Ag)

Initially two Co/Ag (111) multilayers were made for NMR studies. They are listed in table 6.1. The multilayers were grown on an oxidized Si substrate with a base layer of 50 Å Fe. The multilayers were made at Michigan State University using magnetron sputtering with rates of 7.4 Å/s and 8.2 Å/s for Co and Ag layers respectively. Sample 249#14 was previously examined in the department [STE92]. The results from the NMR experiments on sample 249#11 will be discussed here and compared to the results from the other sample and the Co/Ag alloy.

Automatic field sweeps were made with the applied field parallel and perpendicular to the interface plane. In both cases there was one broad line observable. The spectra are very similar to the spectra of sample 249#14.

The difference between the resonance fields ($B_{res,\perp} - B_{res,||}$) is 1.1 ±0.1 T for both samples. This means that the bulk line is not pure fcc or hcp which for some reason has become very broad, because the difference would be about 1.8 T for fcc Co and 0.95 T for hcp Co. The width of the lines at half hight is 1.25 ±0.05 T, which is the same as the width of the total bulk intensity in the spectrum of the alloy. This seems to indicate that the broad bulk contribution is the result of fcc, hcp, and stacking fault structured Co.

A step wise field sweep with the applied field parallel to the interface plane along with a step wise frequency spectrum with zero applied field were made. The field swept spectra were corrected for receiving enhancement and the frequency swept spectra were corrected for the f^2 dependence of the spin echo intensity. Figure 6.3 shows the spectra of both the samples. Both spectra show a satellite line. The detemined hyperfine fields

60×(15 Å Co + x Å Ag)

Batch number	t_{Ag} (Å)
249#11	9
249#14	20

Table 6.1: *The layer thicknesses t_{Ag}, in Å, of the examined multilayers.*

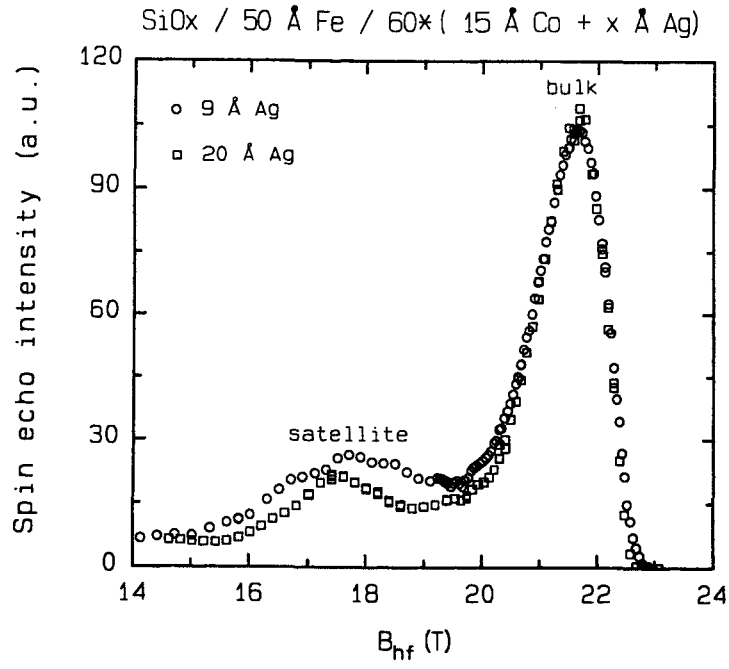

Figure 6.3: *The step wise hyperfine field spectra of the 60×(15 Å Co + 9 Å Ag) and 60×(15 Å Co + 20 Å Ag) multilayers made at 1.4 K. Above 20 T the spectra were determined by field sweeps at 190 MHz with the applied field parallel to the interface plane and are corrected for enhancement. Below 20 T the spectra were determined by zero applied field frequency sweeps and are corrected for the f^2 dependence of the spin echo intensity. The spectra of the two samples are normalized to have the same bulk line hight.*

are listed in table B.5. The average distance between the bulk line and the satellite line is 3.9 ± 0.2 T while that between the fcc bulk line and the satellite in the alloy is 3.1 ± 0.1 T. The majority of this difference can be attributed to the fact that the bulk line from the multilayer is the result of several contributions including fcc Co, which has a lower hyperfine field than the resulting line. The remaining difference might be the result of the fact that outside the nearest neighbor shell, an Co atom in an alloy has a different environment than a Co atom in a multilayer near an interface. Furthermore, because different methods were used to determine the parts of the spectum, caution is needed when determining the differences in the hyperfine fields (see chapter 4).

As figure 6.3 clearly shows, the satellite (interface) intensity of the two samples is not the same. The sample with 9 Å Co appears to have more interface signal, thus having apparantly a different interface in comparison to the other sample.

6.1.3 100×(x Å Co + y Å Ag)

Two series of a total of 16 Co/Ag (111) multilayers were grown. Twelve of these samples were studied with NMR. These samples are listed in table 6.2. The first series has Co layer thicknesses varying from 10 to 100 Å, while the Ag layer thickness is 20 Å. The second series has Co thicknesses of 20 Å, while the Ag layer thickness varies from 9 to 100 Å.

Series 1 100×(x Å Co+20 Å Ag)		Series 2 100×(20 Å Co+y Å Ag)	
sample number	t_{Co} (Å)	sample number	t_{Ag} (Å)
396-2	100	397-10	100
396-4	40	397-12	40
396-6	30	397-14	28
397-9	20	397-9	20
397-8	15	397-15	16
396-7	12	397-13	9
396-5	10		

Table 6.2: *The layer thicknesses t_{Co} and t_{Ag}, in Å, of the examined multilayers.*

The samples were made at Michigan State University using magnetron sputtering. The substrate is Si(100) and the base layer is 50 Å Ag. There is a top layer of also 50 Å Ag. The Co and Ag layers were grown at rates of 4 Å/s and 8 Å/s respectively with a substrate temperature of -20 °C.

Automatic field sweeps were made of all the samples with the applied field parallel to the interface plane at frequencies of 180 and 190 MHz for series 1 and only at 190 MHz for series 2. All spectra were corrected for enhancement. Figure 6.4 shows the spectra of samples (100 Å Co + 20 Å Ag) and (40 Å Co + 20 Å Ag). The spectrum of sample (40 Å Co + 20 Å Ag) is typical for all the other spectra and similar to those discussed in the previous section. There is one very broad line. On the high field side of this line, the intensity decreases to zero. On the low field side, there remains some intensity, probably from the interface. Because the shape of the bulk line for all the other samples is the same, it seem as if the structure of these multilayers is also the same. The spectrum of sample (100 Å Co + 20 Å Ag) gives additional proof for the conclusion concerning the very broad line in the other spectra made in the previous section, which stated that the multilayers contain fcc, hcp, and stacking fault structured Co. In this spectrum the fcc line can clearly be distinguished from the other contributions. It seems that in the case of the other samples, the fcc Co contribution is decreased with respect to the stacking fault Co contributions, thus no longer separately distinguishable

In figure 6.5 the spectra of the same samples but made with the applied field perpendicular to the interface plane are shown. Again the spectrum of sample (40 Å Co + 20 Å Ag) is typical for all the other spectra. The spectrum of sample (100 Å Co + 20 Å Ag) is again slightly different, although the lines are no longer separately identifiable.

The hyperfine fields of the bulk lines were grafically determined from the spectra made with the applied field parallel to the interface plane. Because the structure of the multilayers seems to be the same, with one execption, a comparison of the hyperfine field can be made. The results as a function of the ratio between the Ag and Co layer thicknesses are shown in figure 6.6 (see also table B.6). There is a clear shift to lower hyperfine fields for series 1 as the Co layer thickness decreases. This shift is opposite in direction to the shift observed in the Co/Ni multilayers, which is expected because the lattice constant of Co is larger than that of Ni ($\Rightarrow$ compressive strain) but smaller than

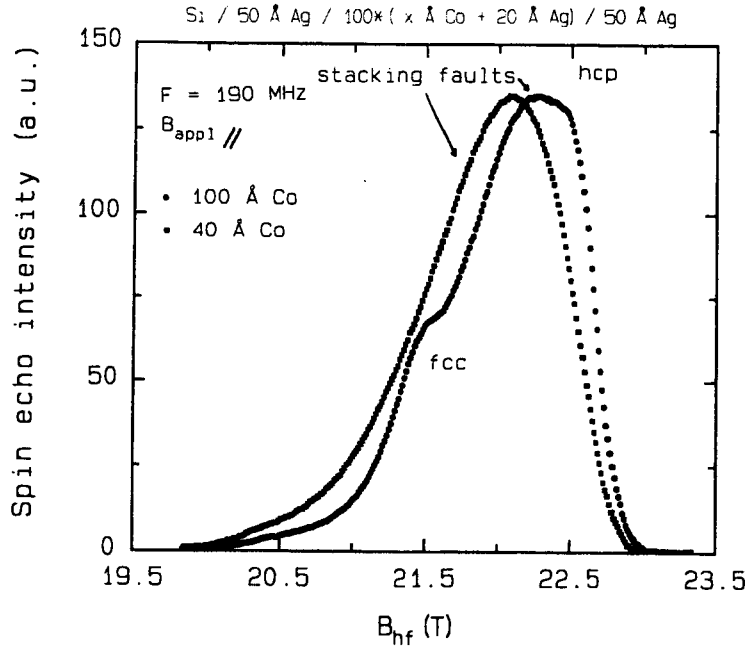

Figure 6.4: *The automatic field swept hyperfine field spectra of the 100×(100 Å Co + 20 Å Ag) and 100×(40 Å Co + 20 Å Ag) multilayers made at 190 MHz with the applied field parallel to the interface plane and at 1.4 K. The spectra are corrected for receiving enhancement and are normalized to have the same bulk line hight.*

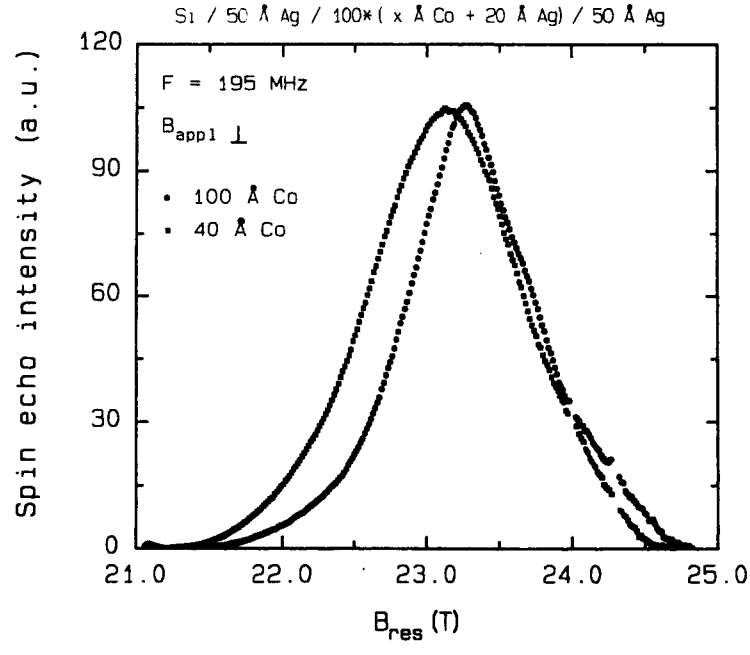

Figure 6.5: *The automatic field swept resonance field spectra of the 100×(100 Å Co + 20 Å Ag) and 100×(40 Å Co + 20 Å Ag) multilayers made at 195 MHz with the applied field perpendicular to the interface plane and at 1.4 K. The spectra are corrected for receiving enhancement and are normalized to have the same bulk line hight.*

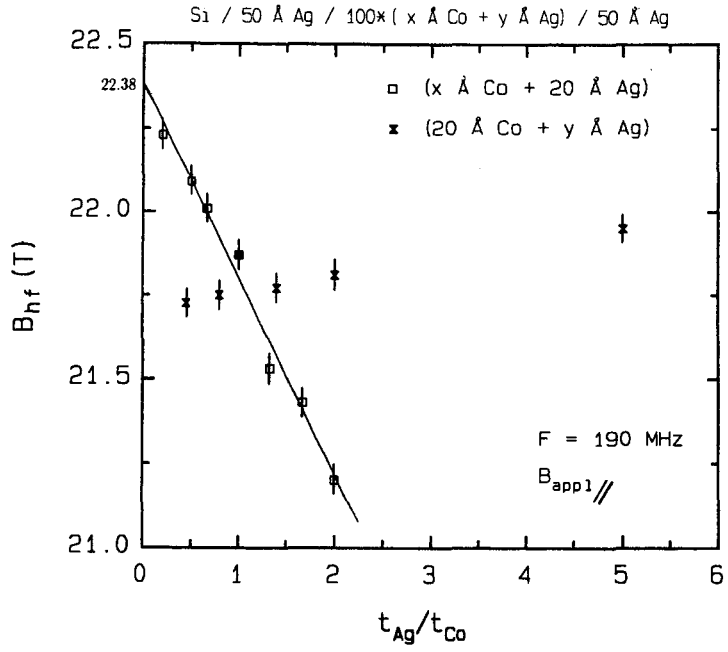

Figure 6.6: *The hyperfine fields of the bulk lines determined from the spectra of the multilayers of the 100×(x Å Co + 20 Å Ag) and 100×(20 Å Co + y Å Ag) series as a function of the ratio between the layer thicknesses t_{Ag}/t_{Co}. The spectra were made at 190 MHz with the applied field parallel to the interface plane, and at 1.4 K. The line is the fit of the data points from the 100×(x Å Co + 20 Å Ag) series.*

that of Ag (⇒ tensile strain).

For series 2 the hyperfine fields are slightly scattered around an almost horizontal line as a function of the ratio t_{Ag}/t_{Co}. It is not clear whether or not there is a dependence of the hyperfine field in the Ag layer thickness or not. It is clear that as a function of the Ag layer thickness, the shift of the hyperfine field is very different from that as a function of the Co layer thickness. Thus, these results show that the Co/Ag multilayers do not have coherent strain.

The critical thickness was calculated using the method described in section 3.2.5 for both series. For series 1, the critical Co layer thickness is 2 Å when the Ag layer thickness is 20 Å. The critical Ag layer thickness is 7 Å when the Co thickness is 20 Å. The elastic and lattice constants used in these calculations are listed in tables C.1 and C.2. Thus, the model predicts that the multilayers studied are incoherent. The results confirm these predictions because they definitely cannot be described by the model for a coherent strain, as the Co/Ni multilayers could.

In figure 6.7 the experimental results are compared to the model for incoherent strain as described in section 3.2.4. Because the hyperfine field values are values that represent a broad line which is actually the envelope of several resonance lines, there is no bulk reference value available with which to compare the results. By extrapolation a line through the data points of series 1 to t_{Ag}/t_{Co}=0 (see figure 6.6), a bulk reference hyperfine field value was determined. This value, $B_{hf,ref}$=22.38 ±0.04 T, is used to calculate the relative hyperfine field shift $\Delta B_{hf}/B_{hf}$, which is proportional to the strain,

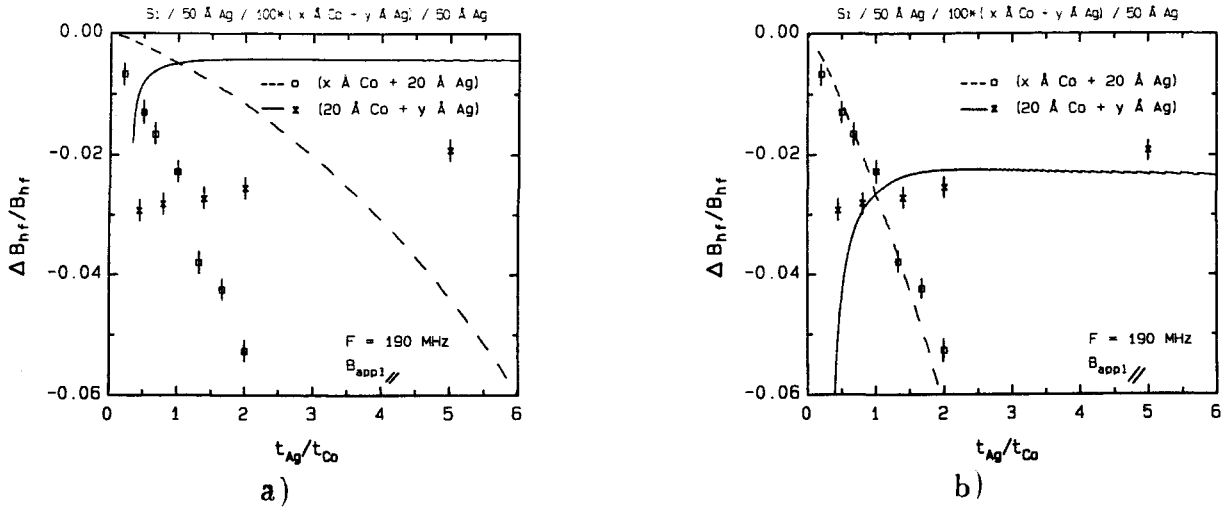

Figure 6.7: *The relative hyperfine field shift $\Delta B_{hf}/B_{hf}$ determined with respect to the bulk reference field, 22.38 T, for the multilayers of the 100×(x Å Co + 20 Å Ag) and 100×(20 Å Co + y Å Ag) series as a function of the ratio between layer thicknesses, t_{Ag}/t_{Co}. The hyperfine fields were determined as in figure 6.6. a) The lines represent the relative hyperfine field shift as calculated with the incoherent strain model for both series. b) The lines represent the relative hyperfine field shift as calculated with the incoherent model for both series and multiplied by 5.35. The jagged line in the calculation for the variable Ag layer thickness series is the result of numerical errors made when determining the strain (see also figure 3.6).*

as in figure 6.7. The relative hyperfine field shift for the sample from series 1 with 10 Å Co is 0.053 ±0.004, which means that the Co lattice constant in the interface plane has increased by (4.3 ±0.3)% and perpendicular to the interface plane it has decreased by (3.8 ±0.3)% (see equations (3.10) and (3.12) to (3.15)).

Both the results and the model show that there is almost a linear dependence of the strain as a function of $1/t_{Co}$ for series 1. However, the strain measured is much larger than that predicted by the model. The error in the hyperfine field value of the sample with t_{Co}=100 Å is slightly larger than that of the other samples because, as mentioned before, the resonance line had a different shape.

Within the Ag layer thickness range of the samples of series 2, the model predicts very little dependence of the strain on the Ag layer thickness. Although the data points are slightly scattered, they seem to follow the behavior shown by the calculations (figure 6.7).

Because there are hardly any variations ($\leq$0.02 T) in the resonance fields of series 2 when the applied field is perpendicular to the interface plane, it is possible that the scatterings in the hyperfine field determined with the applied field parallel to the interface plane are the result of experimental errors. The spectra were made with automatic field sweeps where the resonance condition was satisfied only at one point in the spectrum. Because the bulk line is so broad, it can be expected that the shape of the line is distorted in an automatic sweep. This, of course, also applies to the spectra made with the field perpendicular to the field plane. Step wise field sweeps are advisable in order to eliminate this possibility.

Another reason for the scattering of the data points of series 2 could be the result

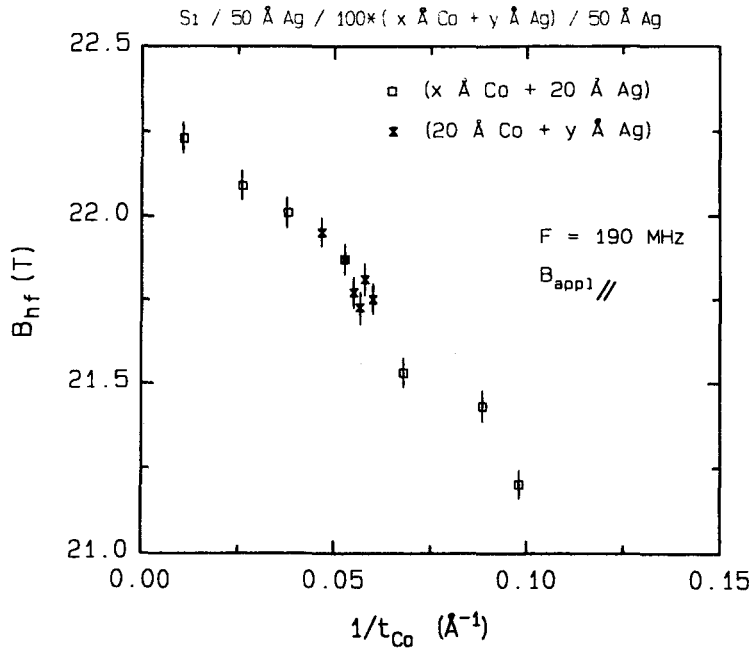

Figure 6.8: *The hyperfine fields of the bulk lines determined from the spectra of the multilayers of the 100×(x Å Co + 20 Å Ag) and 100×(20 Å Co + y Å Ag) series as a function of $1/t_{Co}$ and where the Co layer thickness was determined from the VSM measurements of the same samples. The spectra were made at 190 MHz with the applied field parallel to the interface plane, and at 1.4 K.*

of the fact that the Co layer thicknesses are not all exactly the same for all the samples. Magnetization measurements (VSM) also show a scattering in the determined values of the magnetic moment. This scattering could be the result of differences in the Co layers thicknesses amoung the samples. Assuming that the variations in the magnetic moments are purely the result of variations in the Co layer thicknesses, the Co thickness of each sample has been determined (see table B.6). The hyperfine field as a function of $1/t_{Co}$ which was determined in this way for both series is shown in figure 6.8. Because there is such a strong dependence of the hyperfine field on the Co layer thickness, it is very possible that part of the scattering of the hyperfine fields of series 2 is the result of varying Co layer thicknesses amoung the sample.

6.2 Conclusions

Both the alloy and the multilayers studied have Co structures which consist of fcc, hcp, and stacking faults. In the case of the alloy and the (100 Å Co + 20 Å Ag) multilayer, the different structures can be clearly observed in the spectra. In the case of the other samples, only one broad line, which is the envelope of these resonance lines is observed. A satellite line was determined for the Co/Ag alloy and two of the multilayers at approximately the same distance from the bulk line. It is not yet clear whether it is a contribution of Co atoms with one or with more Ag nearest neighbors.

The Co/Ag multilayers show a strong dependence of the strain as a function of the

Co layer thickness and no apparent dependence on the Ag layer thickness. The fact that the spectra were made with automatic field sweeps, which can cause distortions in the shape of the lines at a distance from the optimalization point, and possible small shifts of the structure of the Co, can be the cause of some errors in the determined hyperfine field values. As mentioned before, the variations in the hyperfine field of the samples of series 2 could also be the result of different Co layer thicknesses. Only if the real layer thicknesses are known, a possible Ag layer thickness dependence can be detected. However, it is clear that any variation of the strain as a function of the Ag layer thickness will be very small, much smaller than that as a function of the Co layer thickness.

It is clear by the dependence of the strain on the layer thicknesses that the layers do not exhibite coherent strain. Considering the fact that the misfit between Co and Ag is 14% this result is expected. Qualitatively the incoherent strain model can describe the results.

For multilayers of for example Co and an other element, the previously used, first order approximation incoherent strain model [MER91], predicted no dependence of the strain on the other layer thickness. The incoherent strain model of Van der Merwe *et al.* [MER88, JES88] shows that especially for thicknesses just above the critical layer thickness (see figure 6.7), the strain does depend on the layer thickness of the other element, while for thicker layers it is again almost independent of it. The incoherent model of Van der Merwe *et al.* seems be an improvement in this respect.

Although qualitatively the model describes the results, the variation in the strain as a function of the Co layer thickness is much larger (about 5 times) than the model predicts. As mentioned in section 3.2.6, there are several reasons why a quantitative agreement between the results and the model is not very likely. The most important reasons are that the model is for cubic non metalic materials and for small misfits between the layers, while the Co and Ag are metals with a large misfits and that besides fcc Co, there is hcp structure and there are stacking faults present in the multilayers.

There are some adaptations of the model that should improve the agreement with the experiments. First of all, a model for the interfacial potential should be used which is appropiate for metals. Van der Merwe *et al.* use parabolic arcs to describe this potential, which they state as not being appropriate for metals. Furthermore, the model should be made to take into account the possibilities of not perfectly smooth interfaces.

Finally, when applying the model correct values of the elastic and lattice constants and information about the elastic behavior of the materials in the multilayer at the temperatures at which the experiments are done is necessary.

The NMR measurements done on the two large Co/Ag multilayer series are only preliminary measurements. These two series are very appropriate for further investigation of several multilayer properties. By making step wise field sweeps, more accurate bulk line resonance fields are possible. Furthermore, a step wise study of the interface intensity could be very interesting. An comparison of the interface and bulk intensities as a function of the Co layer thickness could give information about the interface roughness. The occurance of pinholes through the Ag layers can be studied by comparison of these intensities as a function of the Ag layer thickness.

Chapter 7

Co/Cu Multilayers

Two Co/Cu multilayers were studied with NMR. Instead of determining the resonance lines of the Co atoms, the resonance lines of the Cu atoms were studied. The Co resonance lines of one of the samples has been previously examined [HEI93]. There are two reasons for these Cu resonance experiments. First of all, there is a desire to gain experience with NMR of non-Co nuclei. Cu does not have a magnetic moment, and thus the resonance field depends only on the frequency and gyromagnetic ratio, $B_{res} = 2\pi f/\gamma$. Cu has two natural isotopes, ^{63}Cu and ^{65}Cu, which have different nuclear gyromagnetic ratios. $\gamma/2\pi$ is equal to 11.285 and 12.089 for ^{63}Cu and ^{65}Cu respectively. Because Cu does not have a magnetic moment, the induced field $\vec{B}_{ind}$ is no longer negligable. The induced field is called the Knight shift in the case of metals, and is the result of the interaction between the nuclear spin and the spins of the conduction electrons. The Knight shift of ^{63}Cu is about -0.24 % [CAR77]. Thus for an applied field of about 4 T, a shift of the resonance line of approximately 0.01 T to a lower field can be expected.

The second reason for these experiments is the desire to investigate the influence of the polarization of the Cu conduction electrons, on the Cu resonance line. This desire is prompted by the large interest in Co/Cu multilayers because of the giant magnetoresistance observed in them, which depends on the electronic states of the Cu conduction electrons. In a Co/Cu multilayer, there is an interaction (indirect magnetic exchange coupling) between the magnetic moments of the Co atoms, in different layers, through a spacially oscillating spin polarization of the conduction electrons of the Cu atoms in the layer inbetween [GOT92, LAN72]. This spin polarization of the conduction electrons will cause a shift in the resonance field of Cu that depends in sign and magnitude on the distance of the Cu atoms to the interface. The effect will be largest for Cu atoms close to the interface.

100×(20 Å Co + x Å Cu)	
Sample number	t_{Cu}
COCU0001	20
COCU0003	9

Table 7.1: *The layer thicknesses t_{Cu}, in Å, of the examined multilayers.*

7.1 Results

The two samples which were studied are listed in table 7.1. The multilayers were ion beam sputtered at Philips Research Laboratories on a substrate of polyester and a base layer of 200 Å Cu. The original samples were circular films with a diameter of 7.5 cm which were cut into about 20 pieces of approximately 1×2 cm. These pieces were stacked on top of each other to make the samples appropriate for the experiments. For sample COCU0001 it was determined, with x-ray diffraction, that the layer thickness decreased towards the edge of the original sample with 5% and 9% for the Co and Cu layers respectively.

Automatic field swept spectra were made of the samples with the applied field parallel to the interface plane. Of sample COCU0001 spectra were made at frequencies of 53 and 61 MHz. Of sample COCU0003 spectra were made at frequencies of 61 and 65 MHz. Also a spectrum with the applied field perpendicular to the interface plane was made of sample COCU0003 at a frequency of 61 MHz. These frequencies were the highest frequencies for which the resonance line of ^{63}Cu appeared at an applied field lower than 6 T, which is the maximum field that the magnets used can produce. A Ag coil, instead of a Cu one was wrapped around the sample for these experiments.

Figures 7.1 and 7.2 show the spectra of the two samples with the applied field parallel to the interface plane and f=61 MHz. both spectra were determined with the same pulse time τ_p. Because the spin echo intensity was small, partially as the result of the low frequency, the signal to noise ratio is small. The resonance fields of both isotopes, determined grafically from the spectra, agree within the error margin of 0.01 T with $2\pi f/\gamma$ (see table B.7). Because the error is in the same order of magnitude as the Knight shift, the Knight shift can not be distinguished. Similar measurements with a Cu coil were made which resulted in a much stronger signal, thus increasing the signal to noice ratio, as the result of the Cu in the coil (see figure 7.3). In this spectrum the experimental error was smaller (± 0.003 T) and the resonance lines of Cu were, within this error margin, 0.01 T lower than $2\pi f/\gamma$, most likely as the result of the Knight shift.

It is obvious that the two lines in the COCU0001 spectrum are broader than those in the COCU0003 spectrum. They are about twice as broad. It is not clear what the exact origin of this difference in line width is. Possible causes could be differences in the structure in the two multilayers, or the spin polarization of the conduction electrons which is influenced by the structure and the interface topology, which could be different in the two multilayers.

The spectrum of sample COCU0003 made with the applied field perpendicular to the interface plane is similar to that made with the applied field parallel. The resonance fields of the lines are the same, as is to be expected because Cu does not have a magnetic moment, thus there is no dipolar interaction.

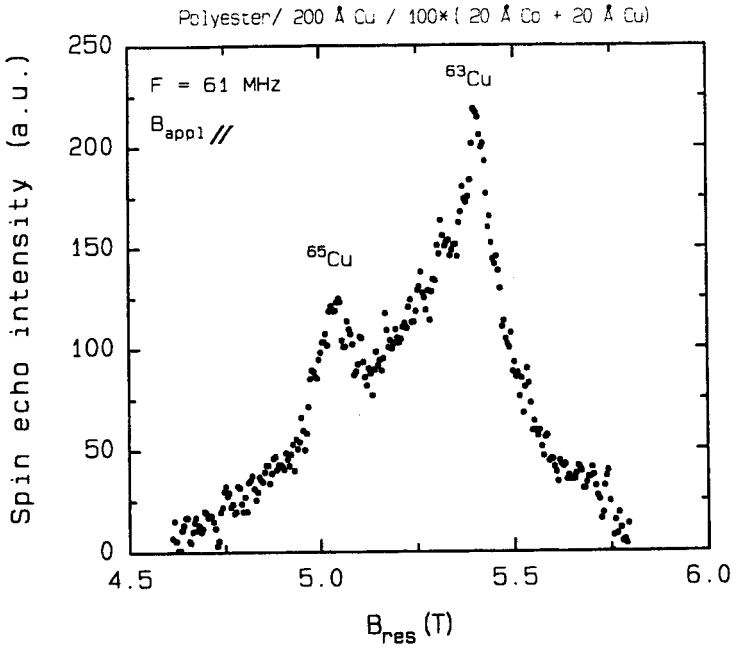

Figure 7.1: *The automatic field swept resonance field spectrum of the 100×(20 Å Co + 20 Å Cu) multilayer made at 61 MHz with the applied field parallel to the interface plane, and at 1.4 K. The spectrum is corrected for receiving enhancement.*

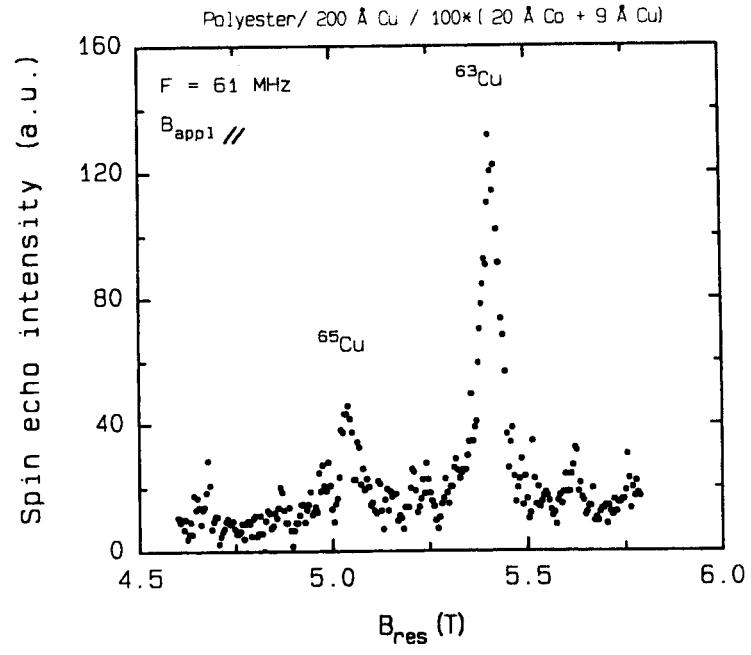

Figure 7.2: *The automatic field swept resonance field spectrum of the 100×(20 Å Co + 9 Å Cu) multilayer made at 61 MHz with the applied field parallel to the interface plane, and at 1.4 K. The spectrum is corrected for receiving enhancement.*

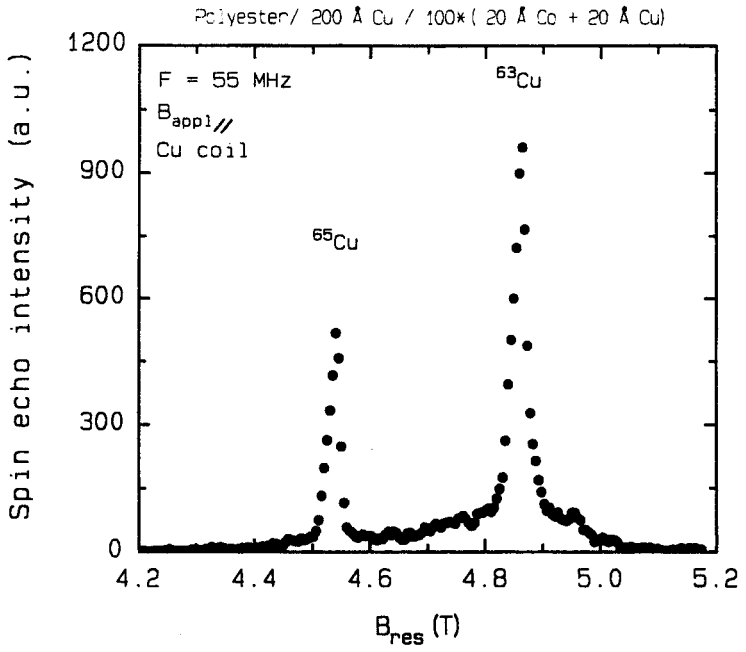

Figure 7.3: *The automatic field swept resonance field spectrum of the 100×(20 Å Co + 20 Å Cu) multilayer made at 55 MHz with the applied field parallel to the interface plane, at 1.4 K, and made using a Cu coil. The spectrum is corrected for receiving enhancement. At this frequency, $2\pi f/\gamma$ is 4.874 and 4.550 T for ^{63}Cu and ^{65}Cu, respectively. The determined resonance fields are 4.862 and 4.540 ±0.003 T, respectively.*

7.2 Conclusions

It is possible to measure with NMR the resonance lines of both Cu isotopes in a Co/Cu multilayer at the expected resonance field. The origin of the difference in the line width in the spectra of the two samples is not yet known. Further investigation of samples with various Cu thicknesses is advisable. In order to be able to distinguish the effects of spin polarization, it is important that the multilayers that are studied have the same structures and interface topologies.

Bibliography

[ALP93] E.A.M. van Alphen, H.A.M. de Gronckel, P.J.H. Bloemen, A.S. van Steenbergen, and W.J.M. de Jonge, J. Magn. Magn. Mater. **121** 77 (1993)

[ABR62] A. Abragam, *The Principles of Nuclear Magnetism*, Oxford Clarendon Press (1962)

[ADA68] R. Adams and C. Altstetter, Trans. Met. Soc. AIME, **242** 139 (1968)

[BLO92] P.J.H. Bloemen, W.J.M. de Jonge, and F.J.A. den Broeder, J. Appl. Phys. **72** 4840 (1992)

[BLÜ87] S. Blügel, H. Akai, R. Zeller, and P.H. Dederichs, Phys. Rev. B **35** 3271 (1987)

[BOR92] R.J. Borg and G.J. Dienes, *The Physcial Chemistry of Solids*, Academic Press (1992)

[BRE30] G. Breit, Phys. Rev. **35** 1447 (1930)

[BR092] F.J.A. den Broeder, E. Janssen, W. Hoving, and W.B. Zeper, IEEE Trans. Magn. **28** 2760 (1992)

[CAR77] G.C. Carter, L.H. Bennett, and D.J. Kahan, *Metallic Shifts in NMR* Progress in Material Science, vol.20, Pergamon Press (1977)

[COL71] J.H.P. Colpa, Physica **56** 185 (1971)

[CUL78] B.D. Cullity, *Elements of X-ray Diffraction*, 2nd ed., Addison-Wesley (1978)

[DAA92] G.H.O. Daalderop, P.J. Kelly, and F.J.A. den Broeder, Phys. Rev. Lett. **68** 682 (1992)

[DEN82] C.J.M. Denissen, Internal report, TUE (1982)

[EBE88] H. Ebert, Phys. Rev. B **38** 9390 (1988)

[FEK76] D. Fekete, A. Grayevskey, D. Shaltiel, U. Goebel, E. Dormanni, N. Kaplan, Phys. Rev. Lett. **36** 1566 (1976)

[FEK78] D. Fekete, H. Boasson, A. Grayevskey, V. Zevin, and N. Kaplan, Phys. Rev. B **17** 347 (1978)

[FER30] E. Fermi, Z. Phys. **60** 320 (1930)

[FEY63] R.P. Feynman, R.B. Leighton, and M. Sands, *The Feynman Lectures on Physics*, vol. 2, Addison-Wesley (1963)

[FRE65] A.J. Freeman and R.E. Watson, in *Magnetism*, edited by G.T. Rado and H. Suhl, Academic Press, New York, Vol. 2A (1965)

[GOT92] A. Goto, H. Yasuoka, H. Yamamoto, and T. Shinjo, "NMR Study of Copper in [Ni/Cu] Magnetic Superlattices, submitted to J. Magn. Magn. Mater. (1992)

[GRO91] H.A.M. de Gronckel, K. Kopinga, W.J.M. de Jonge, P. Panissod, J.P. Schillé, and F.J.A. den Broeder, Phys. Rev. B **44** 9100 (1991)

[GRO92] H.A.M. de Gronckel, W.J.M. de Jonge, *NMR Studies on Magnetic Multilayers*, to be published in a volume on magnetic multilayers, edited by L.H. Bennet and R.E. Watson, World Scientific (1992)

[GRO92b] H.A.M. de Gronckel, B.M. Mertens, P.J.H. Bloemen, K. Kopinga, and W.J.M. de Jonge, J. Magn. Magn. Mater. **104-107** 1809 (1992)

[GRO93] H.A.M. de Gronckel, Ph.D. thesis, yet to be published (1993)

[HAH50] E.L. Hahn, Phys. Rev. **80** 580 (1950)

[HEI93] P. van der Heijden, Internal report, TUE (1993)

[HOU76] D.I. Hoult and R.E. Richards, J. Magn. Reson. **24** 71 (1976)

[JAN79] J.F. Janak, Phys. Rev. B **20** 2206 (1979)

[JAS90] J.A. Jaszczak, S.R. Phillpot, and D. Wolf, J. Appl. Phys. **68** 4573 (1990)

[JES88] W.A. Jesser and J.H. van der Merwe, J. Appl. Phys. **63** 1928 (1988)

[KLE87] H. Kleuskens, Internal report TUE (1987)

[LAF61] R.C. La Force, S.F. Ravitz, and G.F. Day, Phys. Rev. Lett. **6** 226 (1961)

[LAN67] Landolt-Börnstein, *Numerical Data and Functional Relationships in Science and Technology*, New Series II/5 Springer-Verlag (1967)

[LAN72] D.V. Lang, J.B. Boyce, D.C. Lo, and C.P. Slichter, Phys. Rev. Lett. **29** 776 (1972)

[LAN86] Landolt-Börnstein, *Numerical Data and Functional Relationships in Science and Technology*, New Series III/19a Springer-Verlag (1986)

[LAN88] Landolt-Börnstein, *Numerical Data and Functional Relationships in Science and Technology*, New Series III/14a Springer-Verlag (1988)

[MER88] J.H. van der Merwe and W.A. Jesser, J. Appl. Phys. **63** 1509 (1988)

[MER91] B.M. Mertens, Internal report TUE (1991)

[PEL86] L. Pel, Internal report TUE (1986)

[PER65] G.J. Perlow, C.E. Johnson, and W. Marshall, Phys. Rev. A **140** 875 (1965)

[PLO88] A.J.M. Plompen, Internal Report TUE (1988)

[PRA91] W.P. Pratt. Jr.,S.-F. Lee, J.M. Slaughter, R. Loloee, P.A. Schroeder, and J. Bass, Phys. Rev. Lett. **66** 3060 (1991)

[RIE68] P.C. Riedi and R.G. Scurlock, J. Appl. Phys. **39** 1241 (1968)

[RIE79] P.C. Riedi, Phys. Rev. B **20** 2203 (1979)

[RIE87] P.C. Riedi, T. Dumelow, M. Rubinstein, G.A. Prinz, S.B. Qadri, Phys. Rev. B **36** 4595 (1987)

[SLI90] C.P. Slichter, *Principles of Magnetic Resonance*, Springer-Verlag Berlin, 3^{rd} ed. (1990)

[SMI76] C.J. Smithells and E.A. Brandes, *Metals Reference Book*, Butterworth (1976)

[STE92] A.S. Steenbergen, Internal Report TUE (1992)

[WAL67] R.E. Walstedt, J.H. Wernick, and V. Jaccarino, Phys. Rev. **162** 301 (1967)

[WAT61] R.E. Watson and A.J. Freeman, Phys. Rev. **123** 2027 (1961)

Appendix A

The Dislocation Energy of an Incoherent Multilayer

The energy of the dislocations at the interface per unit area as given by Van der Merwe *et al.* [MER88, JES88] is equal to:

$$\begin{aligned} E_d(t,\bar{\eta}(\bar{e})) &= \frac{cG_a\bar{\eta}}{2\pi(1-\sigma)}\left\{\frac{2}{(R'+r^{-1})L}\left(arctan(L\bar{X}_t)-arctan(L(\bar{X}_t-2))\right)\right. \\ &+\frac{\pm 2}{\sqrt{\pm q}}\left[\begin{matrix}arctan\\arctanh\end{matrix}\left(\frac{K\bar{X}_t+R'}{\sqrt{\pm q}}\right)-\begin{matrix}arctan\\arctanh\end{matrix}\left(\frac{K\bar{X}_t r+R'}{\sqrt{\pm q}}\right)\right] \\ &\left.+\frac{G_+}{G_a}\ln\left(1+\frac{(1-\sigma)trG}{2c\bar{X}_t G_+}\right)\right\} \end{aligned} \tag{A.1}$$

for $r = t_a/t_b \leq 1$ with $\bar{e} = \mid \bar{e}_b \mid$ and $t = t_b$ and where $\bar{e}$ is the misfit strain and t is the layer thickness. When $q > 0$ the + sign and *arctan* apply, and when $q < 0$ the − sign and *arctanh* apply. Furthermore :

$$\bar{\eta} = \eta - \frac{a_a \mid \bar{e}_a \mid + a_b \mid \bar{e}_b \mid}{\frac{1}{2}(a_a+a_b)} = \eta - \frac{2a_b}{a_a+a_b}\left(1+\frac{a_a}{a_b r R}\right)\bar{e}, \text{ the misfit} \tag{A.2}$$

$$c = \frac{2a_a a_b}{a_a+a_b}, \text{ the reference lattice constant} \tag{A.3}$$

$$\frac{1}{G_+} = \frac{1}{G_a}+\frac{1}{G_b} \tag{A.4}$$

$$G = \frac{1}{2}(G_a+G_b), \text{ the shear modulus at the interface} \tag{A.5}$$

$$\sigma = \frac{1}{2}(\sigma_a+\sigma_b), \text{ the Poisson ratio at the interface} \tag{A.6}$$

$$n_i = 0.561 \tag{A.7}$$

$$\bar{X}_t \equiv 2+\frac{n_i\pi t}{c}\bar{\eta} \tag{A.8}$$

$$K \equiv \frac{4cG_a}{(1-\sigma)trG}+\frac{2}{3} \tag{A.9}$$

$$L^2 \equiv \frac{Kr + \frac{2R'}{3}}{R' + r^{-1}} \tag{A.10}$$

$$q \equiv K - R^2 \tag{A.11}$$

$$R' = \frac{G_a}{G_b} \tag{A.12}$$

$$\tag{A.13}$$

and R is given by equation 3.29.

Appendix B

Measured Resonance Fields

B.1 Co/Ni

SiOx/300 Å Au/ 25×(12 Å Co + x Å Ni) (111)

Batch number	Nominal t_{Ni} (Å)	Chemical Analysis (±3%) t_{Ni} (Å)	Chemical Analysis (±3%) t_{Co} (Å)	Resonance field, automatic sweep $B_{appl,\|\|}$ Bulk 190 MHz (T)	$B_{appl,\|\|}$ 1^{st} sat. 180 MHz (T)	$B_{appl,\|\|}$ 2^{nd} sat. 180 MHz (T)	$B_{appl,\perp}$ Bulk 195 MHz (T)	$B_\perp - B_\|$ bulk (T)
910701	4	4.7	13.2	21.58 [1]		20.05	23.46 [2]	1.9 [3]
910702	8	8.0	12.1	21.61		20.15	23.55	1.94
910704	10	10.5	12.6	21.60		20.14	23.59	1.99
910705	12	13.0	12.9	21.63		20.20	23.55	1.92
910706	16	16.0	12.3	21.63		20.21	23.58	1.95
910708	21	21.9	12.9	21.65		20.19	23.58	1.93
910710	30	31.6	13.0	21.65		20.21	23.59	1.94
910711	42	42.6	12.4	21.67		20.25	23.60	1.93
910712	60	60.3	12.6	21.70	20.97	20.27	23.63	1.93
910713	100	103.9	13.5	21.72	20.99	20.30	23.61	1.89
				±0.03	±0.05	±0.02	±0.05	±0.08

Table B.1: *The resonance fields determined from the spectra made with automatic field sweeps at 1.4 K.*

[1] ±0.05 T
[2] ±0.07 T
[3] ±0.1 T

Mica/200 Å Au/ N×(x Å Co + 2x Å Ni) (111)

Batch number	N	x	Chemical Analysis (±3%)		Step wise sweep Resonance field $B_{appl,\|\|}$		
			t_{Co} (Å)	t_{Ni} (Å)	Bulk 190 MHz (T)	nnn 180 MHz (T)	2^{nd} sat. 180 MHz (T)
915104	40	6	5.6	12.5		21.42	20.32
915105	30	8	7.4	16.7		21.45	20.27
915106	24	10	9.2	19.9	21.73	21.48	20.27
915107	20	12	11.2	24.7	21.71	21.45	20.29
915108	15	16	15.5	32.2	21.68	21.45	20.26
915109	10	24	23.2	49.9	21.65		20.24
					±0.03	±0.03	±0.02

Table B.2: *The resonance fields determined from the spectra made with step wise field sweeps at 1.4 K.*

Mica/200 Å Au/ N×(x Å Co + 2x Å Ni) (111)

Batch number	Automatic sweep Resonance field (T)		
	$B_{appl,\|\|}$ 190 MHz	$B_{appl,\perp}$ 195 MHz	$B_\perp - B_\|$
915106	21.74	23.46	1.72
915107	21.72	23.60	1.88
915108	21.70	23.40	1.70
915109	21.64	23.33	1.69
	±0.04	±0.04	±0.08

Table B.3: *The bulk resonance fields determined from spectra made with automatic field sweeps at 1.4 K.*

B.2 Co/Ag

Mica/4×3000 Å (Co + 2% Ag)

Sample Number	Resonance field (T)				
	Aut. field sweep F=190 MHz				Frequency sweep B_{appl} = 0 T
	fcc	s.f.	s.f.	hcp	Satellite
920801	21.54	21.81	22.18	22.51	18.4
	±0.04				± 0.1

Table B.4: *The resonance fields determined from the spectra made with automatic field sweeps and zero applied field frequency sweeps at 1.4 K. S.f. means stacking fault.*

SiOx/50 Å Fe /60×(15 Å Co + x Å Ag)

Sample number	Resonance field (T)					
	Automatic sweep			Step wise sweep		
	Bulk			Bulk	Sat.	Bulk-Sat.
	$B_{\|\|}$ (190 MHz)	$B_{\perp}$ (195 MHz)	$B_{\perp} - B_{\|\|}$	$B_{\|\|}$ (190 MHz)	zero field	
249#11	21.68	22.78	1.1	21.63	17.9	3.7
249#14	21.58	22.72	1.1	21.61	17.6	4.0
	± 0.05	± 0.05	± 0.1	± 0.05	± 0.1	± 0.1

Table B.5: *The resonance fields determined from the spectra made with automatic and step wise field and frequency sweeps at 1.4 K.*

Si(100)/50 Å Ag/100× (x Å Co + y Å Ag)/50 Å Ag (111)

Sample number	t_{Co} (Å)	t_{Ag} (Å)	t_{Co} (VSM) (Å)	Resonance field, automatic sweep Bulk Co			
				$B_{\|\|}$		$B_\perp$	$B_\perp - B_{\|\|}$
				(190 MHz) (T)	(180 MHz) (T)	(195 MHz) (T)	(T)
396-2	100	20	93.4	22.23	22.18	23.27	1.0
396-4	40	20	38.3	22.09	22.06	23.14	1.1
396-6	30	20	26.4	22.01		23.06	1.1
397-9	20	20	19.0	21.87	21.82	22.90	1.0
397-8	15	20	14.7	21.53	21.51	22.59	1.1
396-7	12	20	11.3	21.43	21.47	22.53	1.1
396-5	10	20	10.2	21.20	21.15	22.21	1.0
397-10	20	100	21.4	21.95		22.92	1.0
397-12	20	40	17.3	21.81		22.89	1.1
397-14	20	28	18.2	21.77		22.91	1.1
397-15	20	16	16.7	21.75		22.89	1.1
397-13	20	9	17.7	21.73		22.86	1.1
			±5%	±0.05	±0.05	±0.05	±0.1

Table B.6: *The resonance fields determined from the spectra made with automatic field sweeps at 1.4 K. Also the Co layer thickness as determined from the VSM measurements are listed.*

B.3 Co/Cu

Polyester/200 Å Cu/100×(20 Å Co + x Å Cu)

	t_{Cu} (Å)	Resonance field (T) (± 0.01 T), automatic sweep							
		$B_{appl,\|\|}$						$B_{appl,\perp}$	
		53 MHz		61 MHz		65 MHz		61 MHz	
		^{63}Cu	^{65}Cu	^{63}Cu	^{65}Cu	^{63}Cu	^{65}Cu	^{63}Cu	^{65}Cu
$2\pi f/\gamma$		4.696	4.384	5.405	5.046	5.760	5.377	5.405	5.046
COCU0001	20	4.69	4.39	5.40	5.05				
COCU0003	9			5.41	5.04	5.76	5.37	5.42	5.06

Table B.7: *The Cu resonance fields determined from the spectra made with automatic field sweeps at T=1.4 K.*

Appendix C

Lattice and Elastic Constants

	lattice constant a (Å)	Bulk Modulus K (10^{11}Pa)	$1/K$ $(10^{12}\text{Pa})^{-1}$	Young's Modulus Y (10^{11}Pa)	Shear Modulus G (10^{11}Pa)	Poisson ratio σ	$\frac{\partial}{\partial P}\ln(B'_{hf})$ $(10^{12}\text{Pa})^{-1}$	Ref.
Co (fcc)	3.5445	1.914	5.28	2.089	0.799	0.310		(1)
	3.548 [1]							(2)
	3.544							(3)
		1.830		2.089		0.310		(4)
			5.07				5.92	(5)
	3.544 ±0.002							(6)
Ni	3.5241	1.836	5.4	2.197	0.834	0.304		(1)
	3.52387							(2)
	3.5239							(3)
		1.864		2.192		0.304		(4)
			4.82				8.9	(5)
		1.876		2.192		0.306		(7)
Ag		0.997		0.821		0.363		(4)
		1.036		0.827		0.367		(7)
	4.08626							(8)
Cu	3.61496							(2)
		1.370		1.295		0.343		(4)
		1.378		1.298		0.343		(7)
Au	4.07825							(2)
		1.709		0.775		0.424		(4)
	4.07894 [2]							(8)

Table C.1: *Lattice and elastic constants determine at room temperature.*

[1] T=700-1768 K
[2] T=25 °C

(1) [LAN86]
(2) [BOR92]
(3) [CUL78]
(4) [LAN67]
(5) [GRO93]
(6) X-ray diffraction of a 1000 Å Co film (fcc)
(7) [SMI76]
(8) [LAN88]

The shear modulus can be calculated by:

$$G = \frac{Y}{2(1+\sigma)} \tag{C.1}$$

In the following table (table C.2) the shear modulus was calculated from the averaged values for the Young's moduli and Poisson ratios from table C.1.

	Shear Modulus G $(10^{11}\mathrm{Pa})$
Co	0.797
Ni	0.841
Ag	0.302
Cu	0.483
Au	0.272

Table C.2:

Acknowlegments

I wish to thank all the members of the group Cooperative Phenonena for making the time that I spent, working on the research project described in this report, very enjoyable and worthwhile. A special thanks goes to Erwin van Alphen for his guidance and support during this past year.